3’ Nucleotide Asymmetry Directs miRNA Strand Selection

Jeffrey C. Medley[1], Sumire Kurosu Moriya[1], Huiwu Ouyang[2], Heather Crawshaw[1], Sarah Y. Zhang[1], Ganesh Panzade[1,3], Will J. Sydzyik[1], Joel T. Sydzyik[1,4], Mira Bhandari[1,5], Christopher M. Hammell[2] and Anna Zinovyeva[1]

[1] Division of Biology, Kansas State University. Manhattan, KS.
[2] Cold Spring Harbor Laboratory. Cold Spring Harbor, NY.
[3] Laboratory of Human Retrovirology and Immunoinformatics, Frederick National Laboratory for Cancer Research, Frederick, MD.
[4] University of Kansas School of Medicine, Kansas City, KS.
[5] Department of Molecular Genetics and Cell Biology, University of Chicago. Chicago, IL.

Abstract

During miRNA biogenesis, double-stranded precursors are processed into duplexes comprising functionally distinct strands. The guide strand directs the miRNA-induced silencing complex (miRISC) to complementary mRNA targets, while the passenger strand is degraded. As each strand has different molecular targets, strand selection effectively determines the target repertoire of the miRISC. Previous studies suggest that 5' nucleotide identity and thermodynamic asymmetries determine miRNA strand choice in vitro. However, these guidelines cannot fully explain the observed strand preference of all miRNAs in vivo. Here, we demonstrate a conserved role for 3’ nucleotide asymmetry in facilitating miRNA strand selection in *Caenorhabditis elegans* and human HEK293T cells. Our data show that a favorable 3' nucleotide on miRNA passenger strands can promote selection of the opposing guide strand. We propose that terminal nucleotide asymmetries on both strands of miRNA duplexes promote accurate strand selection in vivo.

Main

The biogenesis of miRNAs is integral to their biological activity, as the precise sequence of mature miRNAs must be preserved to maintain sequence-specific interactions with mRNA targets[1,2]. Primary miRNA (pri-miRNA) transcripts are genomically encoded and processed within the nucleus by the microprocessor complex to produce stem-loop miRNA precursors (pre-miRNA)[3–6]. Following nuclear export, Dicer cleaves pre-miRNAs to generate partially double-stranded ~22 nucleotide duplexes that typically contain two-nucleotide overhangs at their 3' ends[7–12]. The miRNA duplex is subsequently loaded into an Argonaute protein, which selectively anchors a single, mature strand to initiate formation of the miRNA induced silencing complex (miRISC)[13,14]. Although the strands originating from either the 5' (5p) or 3' (3p) arms of the pre-miRNA are competent for Argonaute loading[15–17], asymmetric strand selection usually leads to a dominant guide strand and a less abundant passenger strand that is rapidly degraded after release from Argonaute[18]. For some miRNAs, strand selection occurs in a more symmetrical fashion where both strands appear to function as mature miRNAs[19,20]. Differences in miRNA strand usage have also been observed in different cellular, tissular and developmental contexts, suggesting that strand selection is a regulated process[19,21–24]. As miRNA-dependent gene regulation is sequence dependent, alternative miRNA strand choice is expected to lead to broad changes in target selection. Consistently, aberrant miRNA strand selection has also been reported in several human diseases including cancers, although the mechanisms leading to alternative strand selection in human disease are not fully understood[18].

Argonaute plays a direct role in strand selection and favors loading the duplex end containing a favorable 5' nucleotide (U>A>C>G) and lower thermodynamic stability in vitro[16,17,25,26]. The 5' nucleotide of the guide strand is embedded within a pocket in the MID domain of Argonaute, which has a strong preference for uracil[13,14,25]. Several residues within the Argonaute MID and PIWI domains directly contact the phosphate backbone of the guide strand[13,14] and may serve as a sensor for thermodynamic asymmetry[17]. The twin-drive model postulates that miRNA strand selection can be predicted by modeling the relative effects of 5' nucleotide identity and thermodynamic asymmetry[17]. However, this model fails to explain strand selection of ~25% of miRNAs that have unfavorable 5' nucleotides and more stable 5' ends[18], suggesting that additional asymmetries influence miRNA strand selection in vivo.

Here, we used genome editing to alter endogenous *C. elegans* miRNAs and evaluated the relative contributions of 5' nucleotide identity and thermodynamic asymmetry in vivo. Consistent with previous findings, we show that a 5' uracil is favorable for stand choice, and that unpaired 5' nucleotides are strongly selected regardless of nucleotide identity. We were surprised to find that duplexes with symmetrical 5' nucleotides and thermodynamic end stabilities underwent asymmetric strand selection, suggesting that additional features outside of the 5' end contribute to strand choice. We identified a strong bias for cytosine at the 3' end of passenger strands in *C. elegans*. Mutating the 3' nucleotide of symmetrical duplexes was sufficient to reverse strand selection, suggesting that 3' nucleotide identity influences miRNA strand asymmetry in vivo. In duplexes with asymmetric 5' ends, 3' nucleotide asymmetry had a lesser effect on strand choice, indicating that various nucleotide asymmetries coordinately drive miRNA strand selection. By expressing exogenous miRNA variants in human HEK293T cells, we show that 3' nucleotide asymmetry plays a conserved role in miRNA strand selection, although a 3' cytosine on passenger strands was less preferred in human cells. Collectively, our results support a model where nucleotide asymmetries on both strands of miRNA duplexes promote asymmetric strand selection.

Results

Characterization of *C. elegans* miRNA duplexes

To better understand how 5' nucleotide identity and thermodynamic asymmetries are linked to miRNA strand selection, we profiled the duplex characteristics of *C. elegans* miRNAs (Supplementary Table 1). The preferred guide strand is expected to have a favorable 5' nucleotide and lower 5' end stability than the corresponding passenger strand (Fig. 1A). Consistent with previous observations[27], the majority of *C. elegans* guide strands have a 5' uracil, whereas passenger strands lack an obvious 5' nucleotide bias (Fig. 1B). To examine thermodynamic asymmetry, we used free energy values of *C. elegans* miRNA duplex ends from a previous study[28]. As expected, the average stability of duplex ends corresponding to guide strands was lower than passenger strands (Fig. 1C, Supplementary Table 1). We observed thermodynamic asymmetry when considering the first through fourth terminal nucleotides, with the largest asymmetry observed for three terminal nucleotides (Fig. 1C). Thus, strand selection of *C. elegans* miRNAs is correlated to 5' nucleotide identity and thermodynamic asymmetry.

A favorable 5' nucleotide is not sufficient to drive miRNA strand selection in vivo

To address whether 5' nucleotide identity and thermodynamic asymmetry directly influence miRNA strand choice in vivo, we used genome editing to alter the duplex properties of endogenous *C. elegans* miRNAs. We first examined a series of mutations in the *mir-58a*, *mir-1* and *mir-2* miRNAs that primarily impacted the identity of 5' nucleotides (Fig. 2, Supplementary Table 2). Both strands of the miR-58 duplex have a favorable 5' uracil, whereas only the guide strands of miR-1 and miR-2 have a 5' uracil (Fig. 2). We used RNAcofold to determine how each miRNA variation affected the thermodynamic stability of the terminal three nucleotides for each duplex end[28] (Supplementary Table 3). For all three miRNAs, the guide duplex end has a lower stability than the passenger duplex end (Fig. 2). Based on predictions from the twin-drive model that considers 5' nucleotide identity and thermodynamic asymmetry[17], the four miR-58 mutations (M1-M4) should switch strand selection, the miR-1-M1 mutation should retain normal strand choice, and the miR-2-M1 mutation should choose both duplex strands indiscriminately leading to equal accumulation of both strands (Supplementary Table 4).

To investigate how miRNA mutations affect strand selection, we performed small RNA sequencing in L4-staged animals (Supplementary Tables 5 and 6), a developmental stage where miR-58, miR-1 and miR-2 have relatively high expression[29]. The miR-58-M1 and miR-58-M2 mutations change the 5' uracil of the guide strand to less favorable nucleotides (adenine and guanine respectively), which results in the 5' nucleotide of the guide strand becoming unpaired, thereby modestly reducing duplex end stability (Fig. 2A). In the miR-58-M3 mutation, we introduced a compensatory mutation in the passenger strand that restores base pairing to the 5' adenine variant (Fig. 2A). Our analysis revealed that miR-58-M1 and miR-58-M2 retain normal strand choice, while miR-58-M3 accumulated both duplex strands at near equal levels (Fig. 2A). As the primary difference between the miR-58-M1 and miR-58-M3 mutations is the base-pairing status of the 5' nucleotide, these results suggest that unpaired 5' nucleotides are highly favorable for strand selection and can override a preferrable 5' nucleotide on the other strand. Consistently, the miR-58-M4 mutation, which alters the 3' end of the guide strand to disrupt base-pairing of the 5' nucleotide on the passenger strand, appeared to select the passenger strand although total miR-58 levels were reduced (Fig. 2A).

Both miR-1-M1 and miR-2-M1 mutations change a terminal C:G pair on the passenger end of the duplex into a U:G wobble pair, such that both duplex strands have a symmetrical 5' uracil and similar thermodynamic end stabilities (Figs. 2B and 2C). For the miR-1-M1 mutation, we

observed some accumulation of passenger strand, however, the miR-1-M1 mutation also appeared to affect mature miR-1 levels (Fig. 2B). On the other hand, we found that the miR-2-M1 mutation caused a reversal of miR-2 strand selection (Fig. 2C). Given that the miR-2-M1 mutation has symmetrical 5' nucleotide identity and thermodynamic end stability (Fig. 2C), this suggests that additional factors likely drive asymmetric strand selection of miR-2. Notably, our data show that the twin-drive model poorly predicted the actual strand preference of these miRNA mutants (Supplementary Table 4). We conclude that 5' nucleotide identity directly influences miRNA strand selection in vivo, although favorable 5' nucleotides are not sufficient to drive asymmetric strand choice, particularly when the 5' nucleotide of one strand is unpaired.

Thermodynamic asymmetry is largely dispensable for miRNA strand choice

We next examined mutations affecting thermodynamic asymmetry of *mir-58a*, *mir-1* and *mir-2* (Fig. 3). The miR-58-M5, miR-58-M6 and miR-58-M7 mutations reduce thermodynamic end stability without altering 5' nucleotide identity (Fig. 3A). The twin-drive model[17] predicted each of these mutations, except for miR-58-M6 and miR-1-M2, to switch strands (Supplementary Table 4). Small RNA sequencing of L4-staged animals (Supplementary Tables 5 and 6) showed that the symmetrical miR-58-M5 and miR-58-M6 mutants asymmetrically selected the canonical miR-58 guide strand (Fig. 3A). Furthermore, while miR-58-M7 mutants accumulated some passenger strands, they did not switch strand preference, despite the passenger duplex end having lower stability (Fig. 3A). This observation suggested factors outside 5' nucleotide identity and thermodynamic asymmetry promote strand selection of miR-58.

The more egregious miR-58-M8, miR-58-M9 and miR-58-M10 mutations reduce the stability of the passenger duplex end while also introducing an unfavorable 5' nucleotide to the guide strand (Fig. 3A). The miR-58-M8 and miR-58-M10 mutations both reversed strand selection, demonstrating that there is not a barrier to selecting the miR-58 passenger strand (Fig. 3A). While the miR-58-M9 mutation did not appear to switch strands, we observed a substantial reduction in mature miR-58 levels (Fig. 3A), which was associated with a significant increase in *pri-mir-58* levels, suggesting ineffective processing of *pri-mir-58* (Extended Data Fig. 1A). We did not observe significant changes in the levels or strand selection of the *mir-58* family members *mir-80*, *mir-81* or *mir-82*[30], supporting our observations are specific to *mir-58* (Extended Data Fig. 2).

The miR-1-M2, miR-1-M3 and miR-1-M4 mutations affect thermodynamic asymmetry while also introducing a 5' uracil to the passenger strand; the 5' nucleotide of the miR-1 guide strand is also mutated to a less favorable cytosine in miR-1-M4 mutants (Fig. 3B). We found that the miR-1-M2 and miR-1-M3 mutations both preferred selection of the canonical miR-1 guide strand, while miR-1-M4 asymmetrically selected the passenger strand (Fig. 3B). We observed a reduction in mature miR-1 levels in each of the miR-1 mutants that we generated in this study (Figs. 2B and 3B), possibly due to decreased *mir-1* expression as *pri-mir-1* levels were significantly reduced in miR-1-M4 mutants (Extended Data Fig. 1B). The miR-2-M2 and miR-2-M3 mutations incorporate a favorable 5' uracil to the miR-2 passenger strand, while also introducing cytosines to the 5' end of the miR-2 guide strand that increase the stability of the guide duplex end (Fig. 3C). The miR-2-M2 and miR-2-M3 mutations both resulted in highly asymmetric selection of the miR-2 passenger strand and appeared to increase mature miR-2 levels (Fig. 3C). We observed modest effects on *pri-mir-2* levels in miR-2 mutants, suggesting that any effects on mature miR-2 levels likely occur downstream of miRNA biogenesis (Extended Data Fig. 1C). Notably, the twin-drive model poorly predicted the strand preference of most miRNA mutants (Supplementary Table 4), suggesting additional factors contribute to strand selection in vivo. Absolute quantification of select miRNA mutants agreed with our small

182 RNA sequencing analysis (Extended Data Fig. 3). Further, we observed phenotypes consistent
183 with loss of guide strand activity in strand switching mutants (Extended Data Fig. 4). In the *mir-*
184 *58* family mutant background, the miR-58-M8, miR-58-M9 and miR-58-M10 mutations caused a
185 reduction in adult body size, consistent with loss of *mir-58* function[30] (Extended Data Fig. 4A-B).
186 Similarly, our *mir-1* and *mir-2* mutants showed resistance to levamisole and aldicarb
187 respectively, as previously reported for loss of *mir-1*[31] and *mir-2*[32] function (Extended Data Fig.
188 4C-D).
189
190 To address whether miRNA biogenesis was affected in miRNA mutants, we quantified how
191 each mutation affected isomiR populations. With a few exceptions, most of the miR-58 variants
192 did not significantly affect the distribution of isomiRs for guide or passenger strands compared
193 to controls, suggesting that miRNA mutations do not affect production of the expected mature
194 miRNA (Extended Data Fig. 5, Supplementary Tables 7 and 8). In miR-58-M4, miR-58-M9 and
195 miR-58-M10 mutants, a four-base truncation of the 3' end of the guide strand was more
196 abundant than the canonical guide sequence without affecting isomiRs for passenger strands
197 (Extended Data Fig. 5, Supplementary Tables 7 and 8). Each of these three mutations contain
198 the same CA:UC mutation towards the 3' end of the guide strand (Supplementary Table 2),
199 which may impact processing of these mutants, as we observed for miR-58-M9 (Extended Data
200 Fig. 1A), or could adversely affect the stability of the 3' end of the miRNA within the Argonaute
201 PAZ domain[13,14,33,34] thereby leading to trimming of exposed 3' ends[35,36]. Similarly, the miR-1-M4
202 mutation accumulated a one-base truncation of the 3' end of the canonical guide strand without
203 affecting passenger strand isomiRs, while isomiR populations appeared unaffected for other
204 miR-1 mutants (Extended Data Fig. 6A-B, Supplementary Table 9). The isomiR populations of
205 miR-2 appeared to be more dynamic, including two abundant 3' truncations of passenger
206 strands in wildtype animals (Extended Data Fig. 6C-D, Supplementary Tables 10 and 11).
207 Interestingly, passenger strand isomiRs were reduced in miR-2 mutants compared to wildtype,
208 suggesting increased precision of generating the expected mature sequence (Extended Data
209 Fig. 6C-D). The miR-2-M2 and miR-2-M3 mutants, which asymmetrically select the miR-2
210 passenger strand (Fig. 3F), also altered the isomiR frequency of the miR-2 guide strand
211 (Extended Data Fig. 6C-D). Thus, while most of the miRNA mutants do not significantly affect
212 isomiR populations, changes in isomiR populations were more frequently observed for
213 passenger strands of highly asymmetric miRNAs. It is possible that certain isomiRs have altered
214 duplex properties that promote their own strand selection, thereby leading to their increased
215 representation relative to the corresponding canonical miRNA, without impacting the actual rate
216 of isomiR formation. For example, in miR-2-M2 mutants, the most abundant guide strand isomiR
217 was a truncation of the 5' cytosine resulting in a more favorable 5' adenine (Extended Data Fig.
218 6C-D). Collectively, our data support a model where the identity and base-pairing status of 5'
219 nucleotides promotes miRNA strand selection but is not sufficient to explain strand preference in
220 vivo.
221
222 **Identification of duplex asymmetries associated with miRNA strand choice**
223
224 As we observed asymmetric strand selection for duplexes with symmetrical 5' ends (Figs. 2 and
225 3), we hypothesized that additional duplex features influence miRNA asymmetry in vivo. As we
226 were unable to identify additional asymmetries within the first four nucleotides on the 5' end of
227 guide and passenger strands (Fig. 4A), we next turned our attention to the 3' end of duplexes
228 and identified two nucleotide biases (Fig. 4B). The first bias was an adenine in the third-to-final
229 position of miRNA passenger strands, which was noticeably enriched among the 30 highest
230 expressed miRNAs in L4-staged animals (Fig. 4B) that represent more than 90% of total miRNA
231 reads and have more confident passenger strand annotations[37] (Fig. 4C). As miRNA duplexes
232 typically contain single stranded 2-nucleotide 3' overhangs[38,39], this adenine bias likely reflects

233 base paring to the preferred 5' uracil of guide strands. The second bias was the presence of a 3'
234 terminal cytosine on miRNA passenger strands, which was less frequently observed on guide
235 strands and nearly absent from the 3' ends of highly expressed miRNAs (Fig. 4B). As the levels
236 of many miRNAs are developmentally regulated, we next examined whether this 3' cytosine bias
237 was present throughout animal development or specific to the L4-stage. Using an existing small
238 RNA sequencing dataset[29], we quantified the observed 3' nucleotide identity of miRNA guide
239 and passenger strands throughout *C. elegans* development (Fig. 4D). Throughout animal
240 development, we found that very few guide strands ended with a 3' cytosine, whereas cytosine
241 was among the most frequent 3' nucleotides of passenger strands (Fig. 4D). We hypothesized
242 that 3' nucleotide asymmetry is associated with miRNA strand choice throughout *C. elegans*
243 development.
244
245 **A 3' cytosine on miRNA passenger strands promotes strand selection in *C. elegans***
246
247 To examine whether 3' nucleotide identity influences miRNA strand selection in vivo, we created
248 an additional set of *mir-58* mutations that alter 3' nucleotide identity in the wildtype or
249 symmetrical miR-58-M6 duplexes (Fig. 5, Supplementary Table 2). The passenger strand of
250 miR-58 has a 3' cytosine and the guide strand has a 3' uracil (Fig. 5A). We generated mutants
251 where the 3' nucleotide of both strands were swapped, or the 3' nucleotide of one strand was
252 mutated to produce duplexes containing symmetrical 3' nucleotides (Fig. 5A). While swapping
253 the 3’ nucleotide of the wild type miR-58 duplex in miR-58-M14 mutants was not sufficient to
254 reverse strand selection, swapping the 3' nucleotides of the miR-58-M6 duplex in miR-58-M16
255 mutants reversed strand preference (Figure 5A, Supplementary Tables 5 and 6). This
256 observation suggests a novel role for 3' nucleotide identity in directing miRNA strand choice.
257 Interestingly, in the miR-58-M6 background, we observed near equal levels of both guide and
258 passenger strands for the miR-58-M17 mutant where both strands have 3' cytosine, but
259 asymmetric selection of the miR-58 guide strand in miR-58-M18 mutants where both strands
260 have 3' uracil (Fig. 5A). Thus, a specific preference for 3' cytosine on passenger strands
261 appears to regulate strand selection of miR-58.
262
263 We next examined 3' nucleotide mutations of *mir-2*, which has a 3' guanine on the passenger
264 strand and a 3' cytosine on the guide strand (Fig. 5B). To minimize the effect of 5' nucleotide
265 identity, we mutated the miR-2-M1 duplex where both miR-2 strands have a symmetrical 5'
266 uracil (Fig. 5B, Supplementary Table 1). The miR-2-M4 mutation switches the 3' nucleotides of
267 each miR-2-M1 strand and the miR-2-M5 mutations mutates the 3' nucleotide of the miR-2-M1
268 passenger strand so that both strands have a symmetrical 3' guanine (Fig. 5B). The miR-2-M1
269 mutation reversed strand preference of miR-2 (Figs. 2B and 5B) presumably due to the 3'
270 cytosine on the canonical miR-2 guide strand (passenger strand of miR-2-M1) (Fig. 5B). This
271 passenger strand accumulation in miR-2-M1 was relieved by mutation of the 3’ cytosine on the
272 miR-2 guide strand in miR-2-M4 and miR-2-M5 mutants, consistent with 3' cytosine directing
273 strand selection of mIR-2 (Fig. 5B). Analysis of miR-2 (Extended Data Fig. 6C-D,
274 Supplementary Tables 10 and 11) and miR-58 isomiRs (Extended Data Fig. 5, Supplementary
275 Tables 7 and 8) indicated that the 3' nucleotide variants were processed correctly. Furthermore,
276 introducing a 3' cytosine to either strand of the miR-48 duplex (Supplementary Table 2) led to a
277 small accumulation of the opposing strand without affecting miR-48 processing (Extended Data
278 Fig. 7, Supplementary Table 12). Similarly, introducing a 3' cytosine to the guide strand of miR-
279 71 (Supplementary Table 2) promoted selection of the miR-71 passenger strand without
280 affecting isomiR populations (Extended Data Fig. 7, Supplementary Table 13), indicating that 3'
281 nucleotide identity influences the strand selection of a wide range of miRNAs in vivo.
282

283 The nucleotide composition of 3' overhangs may influence strand asymmetry, as we observed
284 modest differences in strand selection when we swapped 3' nucleotides or the dinucleotide
285 overhangs of miR-58 duplexes (Extended Data Fig. 8). However, we did not identify obvious
286 nucleotide asymmetries beyond the terminal nucleotide of 3' ends, so we chose to focus on the
287 role of 3' nucleotide identity in this study (Fig. 4B). We next asked whether 3' nucleotide identity
288 might be directly recognized by Argonaute. To address this, we mutated a putative 3' nucleotide
289 binding pocket[17] that is positioned near the 5' nucleotide binding pocket in the MID domain[13,14,25]
290 of the *C. elegans* miRNA-associated Argonaute ALG-1 (Extended Data Fig. 9A-B). Although
291 small RNA sequencing did not identify miRNA strand switching in ALG-1^{7A} mutants, we
292 observed accumulation of several miRNA passenger strands (Extended Data Fig. 9C,
293 Supplementary Table 6), suggesting that the interaction between 3' nucleotides and Argonaute
294 may, at least in part, promote accurate strand selection. Collectively, our results suggest that a
295 3' cytosine on miRNA passenger strands promotes guide strand selection and is sufficient to
296 direct strand selection of miRNAs with symmetrical 5' duplex ends.
297
298 **3' nucleotide identity plays a conserved role in directing miRNA choice**
299
300 We next asked whether 3' nucleotide identity influences miRNA strand selection in an
301 evolutionarily conserved fashion. We used the shERWOOD UltramiR system[40] to introduce a
302 set of miR-58 variants into human HEK293T cells (Fig. 6A). The human genome does not
303 encode a miR-58 homolog, which allowed us to track the strand preference of the exogenous
304 miR-58 variants. We first transfected the wildtype miR-58 and symmetrical miR-58-M6 duplexes
305 as well as their respective 3' nucleotide swapped variants miR-58-M14 and miR-58-M16 (Fig.
306 6A). Our small RNA sequencing (Supplementary Table 14) showed that the canonical miR-58
307 guide strand is asymmetrically selected, like what is observed in *C. elegans* (Fig. 6A). However,
308 unlike in *C. elegans*, both strands of the symmetrical miR-58-M6 duplex appear to be selected
309 at near equal frequency (Fig. 6A), suggesting there may be an inherent difference in miRNA
310 strand selection between *C. elegans* and humans. Furthermore, we found that passenger strand
311 levels were reduced in the 3' nucleotide swapped variants miR-58-M14 and miR-58-M16 that
312 each have a 3' cytosine on the miRNA guide strand (Fig. 6A), suggesting 3' cytosine is less
313 favored in human cells. Each of the miR-58 variants appeared to be processed correctly based
314 on isomiR analysis (Extended Data Fig. 10, Supplementary Table 15). However, an additional
315 set of mutations that we designed in a modified version of the human miR-339 duplex were not
316 processed as expected (Extended Data Fig. 10, Supplementary Table 15), despite a modest
317 effect on strand asymmetry by those mutations (Supplementary Table 14).
318
319 To characterize the 3' nucleotide preference in human cells, we created several miR-58-M6
320 duplexes comprising 16 possible 3' nucleotide combinations for each duplex strand (Fig. 6B). To
321 quantify the levels of each miR-58 variant, we performed absolute quantification for each duplex
322 strand (Fig. 6C, Supplementary Table 16). We found that a 3' guanine on the guide (3p) strand
323 of miR-58-M6 and a 3' uracil on the passenger (5p) strand of miR-58-M6 were most favorable
324 for guide strand selection (Fig. 6B). Notably, when each miR-58-M6 strand contained a 3' uracil
325 or adenine, the 3p strand was highly favored whereas when each strand contained a 3' guanine
326 or cytosine the 5p strand was asymmetrically selected (Fig. 6B). These observations suggest
327 that precursor origin may influence miRNA strand choice, or that additional duplex features,
328 such as 3' overhang composition, may play a prominent role in directing miRNA strand choice in
329 human cells. We were unable to identify an obvious nucleotide bias at the 3' end of human
330 miRNA duplexes (Fig. 6C-D, Supplementary Table 17), consistent with the idea that additional
331 duplex features may influence strand asymmetry in human cells. Collectively, our results
332 indicate that 3' nucleotide asymmetry plays an evolutionarily conserved role in regulating miRNA
333 strand choice. While it is unclear how 3' nucleotide asymmetry is recognized, we propose two

alternative hypotheses that are not mutually exclusive, where the 3' nucleotide is directly bound by Argonaute or by an accessory protein to facilitate guide strand selection and passenger strand removal (Fig. 6E).

Discussion

How does 3' nucleotide identity promote miRNA strand choice? One possibility is that Argonaute directly binds to the 5' nucleotide of the guide strand[13,14,25] and the 3' nucleotide of the passenger strand to initiate duplex unwinding (Fig. 6E). Consistent with this idea, we found that mutating a putative 3' nucleotide binding pocket on Argonaute[17] led to an accumulation of some miRNA passenger strands (Extended Data Fig. 9C). It is possible that duplex binding triggers a conformational change of Argonaute that promotes passive wedging by its N-terminal domain[55]. Further, mutations in *C. elegans* ALG-1 and its human homolog Ago2 affect miRNA strand asymmetry[56,57], although it is currently unclear whether those mutations are connected to recognition of 3' nucleotide identity. An alternative, but not mutually exclusive hypothesis is that Argonaute interacts with additional factors that are responsible for recognizing 3' nucleotide identity (Fig. 6E). For example, the Dicer-interacting proteins TRBP and PACT regulate miRNA strand selection in humans[58–60], and Dicer can reposition the miRNA duplex after dicing[59], which could indicate that Dicer may pass miRNA duplexes to Argonaute in a favorable orientation. Notably, the *C. elegans* genome lacks obvious homologs for both TRPB and PACT, which could at least partially explain some of the differences in strand selection and 3' nucleotide preferences that we observed between *C. elegans* and human cells. It is also possible that the protein composition of different strand selection complexes might regulate miRNA strand choice or play a role in sorting duplexes to specific Argonaute proteins that may have different 3' nucleotide preferences. Although 3' nucleotide identity appears to play a conserved role in miRNA strand selection, it is worth noting that human miRNAs, unlike *C. elegans* miRNAs, lack an obvious 3' nucleotide asymmetry. This observation highlights the value of model systems, such as *C. elegans*, in understanding the basic mechanisms of miRNA strand selection, of which our current understanding remains incomplete.

While both regulation and dysregulation of miRNA strand asymmetry have previously been reported (see review[18]), current models of miRNA strand selection lack a dynamic component to explain context-dependent changes in strand preference[17]. As 3' isomiRs are typically more frequent than 5' isomiRs[29,41,42], changes in 3' isomiRs reported in developmental[29,43–45], cellular[46,47] or disease[48] contexts may underly miRNA strand dynamicity. Some 3' modifications, such as miRNA tailing and trimming[36,49], likely occur after strand selection and are not necessarily expected to affect miRNA strand choice. Other 3' modifications, such as adenylation or uridylation, often target pre-miRNA molecules[42,50–52] and are more likely to influence strand asymmetry. Consistently, uridylation of human miR-324 leads to altered strand selection, although uridylation of miR-324 may primarily influence Dicer-dependent processing[53]. Intriguingly, cytidylation of miRNA precursors has been observed in Arabidopsis[54] and the miR-83-3p guide strand is cytidylated in *C. elegans*[49]. As our data indicates that a 3' cytosine on miRNA passenger strands is favorable for strand selection, cytidylation of one strand could promote selection of the other duplex strand. However, modification of miRNA passenger strands may be difficult to detect due to their rapid degradation in cells. Additional work will be needed to fully understand how 3' nucleotide are recognized and how changes in 3' nucleotide identity may regulate miRNA strand selection across different contexts and potentially disrupt strand selection in human disease.

Methods

385 ***C. elegans* Strains and Genetic Analysis**
386
387 A complete list of *C. elegans* strains used in this study is provided in Supplementary Table 18.
388 All strains were derived from the wild-type N2 genetic background. Strains were maintained at
389 20°C under standard growth conditions[61] . Nematode growth medium (NGM) plates that were
390 seeded with *Escherichia coli* OP50 were used as a food source. For developmental stage-
391 specific analysis, animals were synchronized using standard alkaline hypochlorite
392 treatment[62,63] and harvested when most (>90%) of the larval population reached the desired
393 developmental stage. For body length measurements, adult animals were imaged on a Leica
394 DM6 upright microscope. Adobe illustrator was used to quantify body length by measuring the
395 path length of a curved line drawn through the center of the animal from the head to base of the
396 tail. For drug assays, young adult worms were added to plates containing 200 μM
397 levamisole[31] or 1mM aldicarb[32] and scored for paralysis at indicated time intervals. Paralysis
398 was defined as the inability for worms to move in response to a touch stimulus from a platinum
399 wire.
400
401 **Profiling miRNA Duplex Characteristics**
402
403 Mature *C. elegans* and human miRNA sequences were retrieved from miRbase v 22.1[37]. Guide
404 and passenger strand annotations were determined based on which strand had the most
405 reported reads on miRbase. 5' nucleotide information was compiled for 5p and 3p strands.
406 RNAcofold from the ViennaRNA Package 2.0[64] was used for duplex folding and to calculate
407 thermodynamic end stability at 20°C as previously described[28]. Predictions of miRNA strand
408 selection were calculated using twin-drive model of strand selection as previously described[17].
409
410 **CRISPR/Cas9 Genome Editing**
411
412 *Streptococcus pyogenes* Cas9 (IDT, Alt-R® S.p. Cas9 Nuclease V3), single-stranded repair
413 templates (IDT, custom ultramers), crRNA and tracrRNA were commercially sourced. A full list
414 of oligonucleotides used in this study is provided in Supplementary Table 19. Microinjection and
415 screening were performed using *dpy-10* co-conversion as previously described[65]. Cas9 was
416 injected at a final concentration of 2.65 μM and all injection mixes included 200 μM KCl and 7.5
417 μM HEPES [pH 7.4]. All crRNAs were injected at a final concentration of 50 μM, except *dpy-10*
418 crRNA was injected at a final concentration of 5 μM. Equimolar tracrRNA was included in all
419 injection mixes. Single stranded DNA oligonucleotides were used to facilitate homology-directed
420 repair and were included at final concentrations of 6 μM or 3 μM (*dpy-10*).
421
422 **RNA Extraction and Isolation**
423
424 Immediately after sample collection, samples were centrifuged and flash-frozen in liquid
425 nitrogen and stored at -80°C until ready for use. Pellets were thawed in 250 μL RNase-free
426 water (final volume). 1 mL of Trizol (Invitrogen) was added and the mixture was continuously
427 vortexed for 10 minutes. Afterwards, 212 μL of chloroform was added and vortexed for an
428 additional minute. The aqueous and organic layers were separated by centrifugation at 19000 x
429 g for 10 minutes at 4°C. The aqueous phase was then recovered and re-extracted using equal
430 volume of phenol:chloroform:isoamyl alcohol (25:24:1, VWR). The RNA was precipitated for 2
431 hours at -20°C using an equal volume of isopropanol. 1.8 μL of Glycoblue (Invitrogen) was
432 added as a co-precipitant. The RNA pellets were washed using 80% (v/v) ethanol and allowed
433 to air-dry on ice for 10 minutes. The dried pellets were dissolved in RNase-free water and stored
434 at -80°C. RNA concentration was determined using a Nanodrop spectrophotometer.
435

436 **Small RNA Sequencing and Analysis**
437
438 For preparation of small RNA libraries, total RNA was first size selected using a 15% denaturing
439 gel using UreaGel (National Diagnostics) reagents. Single-stranded 18mer
440 (AGCTGCCAGCAACTCTAA) and 26mer (TAGTATGTAGCTGCCAGCAACTCTAA) were
441 combined at a final concentration of 5 µM and used as a molecular ladder in an empty lane.
442 Gels were soaked in 1XTBE solution containing 1X SYBR Gold stain (Invitrogen) for 10 minutes
443 and subsequently visualized under UV light. Small RNAs migrating between the 16mer and
444 26mer markers were excised from the gel and soaked in 750 µL of TE buffer supplemented with
445 0.3 M NaCl overnight while shaking at 550 rpm at 7°C. The solution was transferred to a 0.45
446 µm column and centrifuged at 4°C for 10 minutes at 2500 x g. Small RNAs were precipitated for
447 2 hours at -20°C using equal volume of isopropanol and 10% sample volume 3M NaOAc. 1.5 µL
448 of Glycoblue (Invitrogen) was used as a co-precipitant. The small RNA pellets were washed
449 once using 80% (v/v) ethanol and allowed to air-dry on ice for 10 minutes. The dried pellets
450 were dissolved in 11 µL of RNase-free water. Size-selected small RNA samples were used to
451 make libraries using the Nextflex Small RNA-Seq Kit v3 (PerkinElmer) or the Nextflex Small
452 RNA-Seq Kit v4 (Revvity) according to manufacturer instructions. Please note that the Nextflex
453 Small RNA-Seq Kit v3 (PerkinElmer) was discontinued during this study. We separated small
454 RNA sequencing data acquired from the v3 (Supplementary Table 5) and v4 kits
455 (Supplementary Table 6) and only made direct comparisons for samples that were sequenced
456 using the same kit, as we observed differences in normalized read counts for several miRNAs
457 when using different kits. All small RNA libraries were sequenced at the Kansas State University
458 Integrated Genomics Facility using an Illumina NextSeq 500 instrument at 75 cycles.
459
460 Small RNA sequence data were processed and analyzed as previously described[29] The
461 cutadapt tool[66] was used to process and trim the sequencing reads. The 3' adapter sequences
462 were first removed using the parameters "-a ATCTCGTATGCCGTCTTCTGCTTGX" and
463 demultiplexed using the parameters "e 1 -a file$:barcodes.fasta", where the "barcodes.fasta"
464 contains a list of barcode sequences in fasta format. The 3' primer sequence was then removed
465 from each read using the parameters "-a TGGAATTCTCGGGTGCCAAGGAACTCCAGTCAC".
466 For the Nextflex Small RNA-Seq Kit v3, each end of the processed sequencing reads contained
467 four-nucleotide randomers that were removed using cutadapt. The final four nucleotides of each
468 sequencing read were trimmed using the parameters "-u -4". The first four nucleotides were
469 trimmed using the parameters "-u 4 -m17 -M29", which also removed processed reads that were
470 shorter than 17 or longer than 19 nucleotides. Read quality was examined using the fastqc
471 tool[67]. Reads were aligned to a list of mature *C. elegans* miRNAs using bowtie[68]. The following
472 command was used for bowtie alignments: "-x miR -a --best --strata --norc -v 3", where "miR" is
473 a bowtie build assembled using a fasta file containing all *C. elegans* mature miRNA sequences
474 obtained from miRbase. The samtools tool[69] was used to generate, sort and index bam files to
475 generate read count data. A custom bash script was used to identify and quantify isomiR
476 abundance from fastq files. Normalization (reads per million) was performed by multiplying the
477 number of mapped reads for individual miRNA loci by the total number of mapped miRNA reads
478 divided by one million.
479
480 **qPCR and Absolute Quantification**
481
482 The QuantiNova SYBR Green RT-PCR kit (Qiagen) was used for standard qPCR reactions
483 according to manufacturer instructions. Final reaction volumes were adjusted to 5 µL and 100
484 ng of total *C. elegans* RNA was used as a template. Absolute quantification of miRNAs using
485 Taqman was performed as previously described[70]. Standard curves were first made using
486 known quantities (0.6ng/µL, $0.6x10^{-2}$ ng/µL, $0.6x10^{-4}$ ng/µL, $0.6x10^{-6}$ ng/µL, and $0.6x10^{-8}$ ng/µL)

of commercially purchased (IDT) single-stranded RNA oligonucleotides prepared from a 2 µg/µL stock. All reactions were carried out at a final volume of 10 µL using the Taqman™ MicroRNA Reverse Transcription Kit (Thermofisher) and Taqman™ Universal Master Mix II, no UNG (Thermofisher) according to manufacturer instructions. Custom or predesigned Taqman™ Small RNA Assays (ThermoFisher) were used at 1X final concentration. 1 ng of total *C. elegans* RNA was used as a template for reverse transcription (10 µL reaction volume) and 0.67 µL of the cDNA product was used for experimental Taqman assays. The ABI 7500 Real-Time PCR System (Applied Biosystems) was used to run all qPCR and Taqman reactions. A full list of oligonucleotides and Taqman assays used in this study is provided in Supplementary Table 19.

UltramiR Plasmid Construction

A full list of plasmids used in this study is provided in Supplementary Table 20. Each miRNA variant was cloned into the pLMN-ZsGreen-Neomycin-shRNA vector (transOMIC) and transformed into NEB® Stable Competent *E. coli* (High Efficiency) according to manufacturer instructions. The pJM1 through pJM7 plasmids were created by Gibson assembly of Gblock gene fragments (IDT) (Supplementary Table 19) and HpaI/MluI (NEB) digested pLMN-ZsGreen-Neomycin-shRNA vector using the Gibson Assembly® Cloning Kit (NEB) according to manufacturer instructions. The pJM10 through pJM23 plasmids were created by performing site-directed mutagenesis of the pJM2 plasmid to mutate the nucleotides corresponding to the 3' end of the 5p or 3p strands using the Q5® Site-Directed Mutagenesis Kit (NEB) according to manufacturer instructions. The primers used for site-directed mutagenesis are listed in Supplementary Table 19. All clones were verified by Sanger sequencing prior to transfection

Human Cell Culture and Transfection

Human HEK 293T cells were seeded in 12-well plates containing 1 mL DMEM with 10% FBS and transfected when reaching ~90% confluency. In one tube 1 µg of UltramiR plasmid was added to 100 µL of Opti-MEM™ (Thermofisher) and vortexed. In a second tube, 5 µL of 1 mg/mL polyethylenimine (PEI) reagent was added to 100 µL of Opti-MEM™ (Thermofisher), vortexed and incubated at room temperature for 5 min. The contents of the second tube were subsequently pipetted into the first tube, vortexed and incubated at room temperature for 15 min. The mixture was then carefully added to the cell media dropwise. After 6 hours, the cell media was changed with fresh warmed DMEM with 10% FBS. 48 hours post-transfection, cells were imaged for ZsGreen expression (Supplementary Figure 1), harvested in 1 mL of Trizol (Invitrogen), frozen and stored at -80ºC until use.

Statistical Analysis

R statistical software was used to calculate all statistics. All *P*-values were calculated using two-tailed *t*-tests assuming equal variance among samples. All statistics are presented as mean ± one standard deviation unless otherwise specified.

Data Availability

Small RNA sequencing data files will be made available in the GEO database upon final publication. All strains and plasmids used in this study are available upon request. All other data supporting the findings of this study are available from the corresponding author on reasonable request.

Acknowledgements

We thank members of the Zinovyeva lab for helpful discussions. We thank Hui Tian, Sarah Coffey and Katherine Adams (Hwang) for technical assistance in generating some worm strains, and Alina Akhunova from the Kansas State Integrated Genomics Facility for technical expertise in generating small RNA sequencing data. We are grateful to Anne Hart for sharing *mir-2* mutant strains. Some of the strains used in this study were provided by the *Caenorhabditis* Genetics Center (CGC) which is funded by NIH Office of Research Infrastructure Programs (P40 OD010440). This work was supported by grants from the National Institutes of Health (R35GM124828 to A.Z. and R01GM117406 to C.M.H.), the Kansas INBRE program (P20 GM103418) and the Johnson Cancer Center at K.S.U. J.C.M was supported by a fellowship from the NIH (F32GM148040).

Author Contributions

J.C.M and A.Z. conceptualized and designed the experiments. A.Z and C.M.H supervised the research and acquired funding. J.C.M, S.K, H.O, H.C, S.Z, W.S, J.S and M.B carried out the experiments. J.C.M and A.Z. performed data analysis and interpreted results. J.C.M and G.P performed the required bioinformatics. J.C.M wrote the original manuscript draft, and all other authors edited the manuscript.

Competing Interests

The authors declare no competing interests.

561 **Figure Legends**
562
563 **Figure 1.** Duplex characteristics of *C. elegans* miRNAs. (A) Duplex features associated with
564 miRNA strand selection. The guide (miR) end of typically contains a favorable 5' nucleotide and
565 lower thermodynamic stability than the passenger (miR*) duplex end. The guide strand is shown
566 in maroon, and the passenger strand is shown in gray. U:A pairs are illustrated by an open
567 circle, G:U wobble pairs are indicated by an open circle with a vertical line and G:C pairs are
568 represented by closed circles. The sizes of bulges and mismatched nucleotides are drawn to
569 scale. (B) Quantification of 5' nucleotide identity for *C. elegans* miRNA guide (maroon) and
570 passenger strands (gray). n is given as the number of miRNA duplexes quantified (C)
571 Quantification of the free energy of miRNA duplex ends corresponding to guide (maroon) and
572 passenger (gray) duplex ends. Free energy values were calculated by in silico unwinding[28] of
573 the terminal 1:4 nucleotides of each duplex end.
574
575 **Figure 2.** 5' nucleotide identity influences miRNA strand selection in vivo. (Left) Schematic
576 representations of (A) miR-58, (B) miR-1 and (C) miR-2 duplex mutations that affect 5'
577 nucleotide identity. (A-C) The guide strand is shown in maroon, and the passenger strand is
578 shown in gray. Mutated nucleotides are indicated by red text. U:A pairs are illustrated by an
579 open circle, G:U wobble pairs are indicated by an open circle with a vertical line and G:C pairs
580 are represented by closed circles. Free energy values (kcal/mol) of the terminal three
581 nucleotides (boxed) are shown on each duplex end. The less stable duplex end is marked with
582 an asterisk and highlighted in a light red box. RNAcofold was used to predict duplex structures
583 at 20°C. (Right) Quantification of small RNA sequencing results for (A) miR-58, (B) miR-1 and
584 (C) miR-2. Data are presented as mean ± standard deviation, with each dot representing
585 quantification from a single library using the NEXTFLEX v3 Small RNA Sequencing Kit. Maroon
586 bars correspond to miRNA guide strands and gray bars represent miRNA passenger strands.
587 Normalization was performed by dividing raw read counts by total mapped miRNA reads and
588 multiplying by one million to acquire reads per million (rpm) values.
589
590 **Figure 3.** Thermodynamic asymmetry is dispensable for miRNA strand selection. (Left)
591 Schematic representations of (A) miR-58, (B) miR-1 and (C) miR-2 duplex mutations that affect
592 the relative thermodynamic stability of each duplex end. (A-C) The guide strand is shown in
593 maroon, and the passenger strand is shown in gray. Mutated nucleotides are indicated by red
594 text. U:A pairs are illustrated by an open circle, G:U wobble pairs are indicated by an open circle
595 with a vertical line and G:C pairs are represented by closed circles. Free energy values
596 (kcal/mol) of the terminal three nucleotides (boxed) are shown on each duplex end. The less
597 stable duplex end is marked with an asterisk and highlighted in a light red box. RNAcofold was
598 used to predict duplex structures at 20°C. (Right) Quantification of small RNA sequencing
599 results for (A) miR-58, (B) miR-1 and (C) miR-2. Data are presented as mean ± standard
600 deviation, with each dot representing quantification from a single library using the NEXTFLEX
601 v3 Small RNA Sequencing Kit. Maroon bars correspond to miRNA guide strands and gray bars
602 represent miRNA passenger strands. Normalization was performed by dividing raw read counts
603 by total mapped miRNA reads and multiplying by one million to acquire reads per million (rpm)
604 values.
605
606 **Figure 4.** *C. elegans* miRNA duplex asymmetries. (A) Sequence logo representation of 5'
607 nucleotide frequencies for *C. elegans* miRNA guide (left) and passenger (right) strands. (B)
608 Sequence logo representation of 3' nucleotide frequencies for *C. elegans* miRNA guide (left)
609 and passenger (right) strands. Asterisk indicates the third nucleotide from the 3' duplex end of
610 the passenger strand that is adjacent to the 3' dinucleotide overhang and is expected to base
611 pair to the 5' nucleotide of the guide strand. (A-B) Sequences are given in 5'-3' orientation, with

612 the 5' or 3' terminal nucleotides indicated by a bulbed line above. Sequence logos were created
613 using the weblogo3 server and colors were modified using Adobe illustrator. (C) Cumulative
614 expression of *C. elegans* miRNAs at L4-stage. Each dot represents one miRNA (guide and
615 passenger strands), plotted in order of most abundant to least abundant. The 10 most abundant
616 miRNAs account for ~65% and the 30 most abundant miRNAs represent >90% of all miRNA
617 sequencing reads at the L4 stage. (D) Quantification of 3' nucleotide frequency for miRNA guide
618 (left) and passenger (right) strands throughout *C. elegans* development. Stacked bar graphs
619 represent the normalized abundance of canonical miRNA guide or passenger strands (not
620 including isomiRs) sorted by terminal 3' nucleotide identity. Schematic (top) illustrates an
621 example of a miRNA duplex loaded into Argonaute (gray) and the arrowhead indicates the
622 position of the 3' nucleotide of the guide (left) or passenger (right) strand. Developmental small
623 RNA sequencing data were acquired from a previous study[29].
624
625 **Figure 5.** A 3' cytosine on miRNA passenger strands is favorable for guide strand choice in *C.*
626 *elegans*. (Left) Schematic representations of (A) miR-58 and (B) miR-2 duplex mutations that
627 affect 3' nucleotide identity. (A-B) The guide strand is shown in maroon, and the passenger
628 strand is shown in gray. The nucleotide composition of dinucleotide overhang are shown for
629 each strand. Note that the guide strand of miR-2 has an atypical trinucleotide overhang at its 3'
630 end. Mutated nucleotides are indicated by red text. U:A pairs are illustrated by an open circle,
631 G:U wobble pairs are indicated by an open circle with a vertical line and G:C pairs are
632 represented by closed circles. RNAcofold was used to predict duplex structures at 20°C. (Right)
633 Quantification of small RNA sequencing results for (A) miR-58 and (B) miR-2. Data are
634 presented as mean ± standard deviation, with each dot representing quantification from a single
635 library using the NEXTFLEX v4 Small RNA Sequencing Kit. Maroon bars correspond to miRNA
636 guide strands and gray bars represent miRNA passenger strands. Normalization was performed
637 by dividing raw read counts by total mapped miRNA reads and multiplying by one million to
638 acquire reads per million (rpm) values.
639
640 **Figure 6.** 3' nucleotide identity influences miRNA strand asymmetry in human HEK293T cells.
641 (A) (Left) Schematic representations of exogenous miR-58 duplexes transfected into HEK293T
642 cells that alter 3' nucleotide identity. The canonical miR-58 guide strand (from *C. elegans*) is
643 shown in maroon, and the passenger strand is shown in gray. The nucleotide composition of
644 dinucleotide overhang are shown for each strand. U:A pairs are illustrated by an open circle,
645 G:U wobble pairs are indicated by an open circle with a vertical line and G:C pairs are
646 represented by closed circles. RNAcofold was used to predict duplex structures at 37°C. (Right)
647 Quantification of small RNA sequencing results for transfected miR-58 variants. Data are
648 presented as mean ± standard deviation, with each dot representing quantification from a single
649 library using the NEXTFLEX v4 Small RNA Sequencing Kit. Maroon bars correspond to
650 canonical miRNA guide strands and gray bars represent canonical miRNA passenger strands.
651 Normalization was performed by dividing raw read counts by total mapped miRNA reads and
652 multiplying by one million to acquire reads per million (rpm) values. (B) Absolute quantification
653 of miR-58-M6 duplex variants comprising each combination of 3' nucleotides on each duplex
654 strand. Heatmap illustrates calculated ln(5p/3p) strand ratios where a deeper maroon color
655 indicates preference for the miR-58-M6-3p (guide) strand. The non-transformed 5p/3p strand
656 ratios are given in each box. (C) Sequence logo representation of 5' nucleotide frequencies for
657 human miRNA guide (left) and passenger (right) strands. (D) Sequence logo representation of
658 3' nucleotide frequencies for human miRNA guide (left) and passenger (right) strands. (C-D)
659 Sequences are given in 5'-3' orientation, with the 5' or 3' terminal nucleotides indicated by a
660 bulbed line above. Sequence logos were created using the weblogo3 server and colors were
661 modified using Adobe illustrator. (E) Hypothetical models of how 3' nucleotide identity influences
662 miRNA strand selection. (Top) The MID domain of Argonaute may directly interact with the 5'

663 nucleotide of the guide strand and the 3' nucleotide of the passenger strand. Such interaction
664 may induce a conformational change that promotes duplex wedging and release of the
665 passenger strand. (Bottom) Alternatively, additional factors may interact with miRNA 3'
666 nucleotides to form a strand selection complex. Dissolution of such complex could facilitate
667 guide strand retention within Argonaute and passenger strand removal.
668
669 **Extended Data Figure 1.** Quantification of (A) *pri-mir-58*, (B) *pri-mir-1* and (C) *pri-mir-2* levels in
670 L4-staged miRNA mutants by qRT-PCR. (A-C) Each dot represents one qRT-PCR data point.
671 Each sample was performed in duplicate and at least three independent replicates were
672 included for each mutation. Data were first normalized to α-tubulin (*tba-1*) and subsequently
673 normalized to appropriate PAM or wildtype (WT) controls. The dashed horizontal line indicates
674 the self-normalized average for appropriate controls. Boxes range from the first to third quartile
675 of the data. The thick bar represents the statistical median. Lines extend to the minimum and
676 maximum data point excluding outliers that were defined as 1.5 times the interquartile range.
677 Statistical analysis: *$p<0.05$, ***$p<0.001$.
678
679 **Extended Data Figure 2.** Analysis of miR-58 family miRNAs in miR-58 mutants. (A) Sequence
680 alignment of the *C. elegans* miR-58 miRNA family members. (B-C) Quantification of mature
681 miR-80 levels in L4-staged animals normalized to PAM controls. Libraries were created with the
682 (B) Nextflex v3 small RNA sequencing kit or the (C) Nextflex v4 small RNA sequencing kit. (D-
683 E) Quantification of mature miR-81 levels in L4-staged animals normalized to PAM controls.
684 Libraries were created with the (D) Nextflex v3 small RNA sequencing kit or the (E) Nextflex v4
685 small RNA sequencing kit. (F-G) Quantification of mature miR-82 levels in L4-staged animals
686 normalized to PAM controls. Libraries were created with the (F) Nextflex v3 small RNA
687 sequencing kit or the (G) Nextflex v4 small RNA sequencing kit. (B-G) Data are presented as
688 mean ± standard deviation, with each dot representing quantification from a single library.
689 Maroon bars correspond to canonical miRNA guide strands and gray bars represent canonical
690 miRNA passenger strands.
691
692 **Extended Data Figure 3.** Absolute quantification of miRNA levels in representative miRNA
693 mutants using miRNA Taqman assays. (A-C) Standard curves created using known amounts of
694 guide and passenger strand RNA for (A) miR-58, (B) miR-1 and (C) miR-2. Linear regression
695 and R2 coefficients are indicated for guide (maroon) and passenger (gray) strands. Each dot
696 represents an independently prepared Taqman assay. (D-E) Absolute quantification of both
697 miR-58 strands in (D) L4-staged or (E) embryonic miR-58 mutants. (F-G) Absolute quantification
698 of both miR-1 strands in (F) L4-staged or (G) embryonic miR-1 mutants. (H-I) Absolute
699 quantification of both miR-58 strands in (H) L4-staged or (I) embryonic miR-52 mutants. (D-I)
700 Data are presented as mean ± standard deviation. Each sample was assayed in triplicate and at
701 least three independent replicates were included for each mutation. Each dot represents
702 quantification from a single Taqman assay. Maroon bars correspond to canonical miRNA guide
703 strands and gray bars represent canonical miRNA passenger strands.
704
705 **Extended Data Figure 4.** Phenotypic analysis of miRNA mutants. (A) Representative images of
706 a (top) *mir-80; mir-81 mir-82* triple miR-58 family mutant and (bottom) *mir-80; mir-58; mir-81 mir-*
707 *82* quadruple family mutant illustrates reduced adult body size associated with loss of miR-58
708 family function. (B) Quantification of adult body length in miR-58 mutants in the *mir-80; mir-81*
709 *mir-82* genetic background. Each dot represents one animal. Boxes range from the first to third
710 quartile of the data. The thick bar represents the statistical median. Lines extend to the
711 minimum and maximum data point excluding outliers that were defined as 1.5 times the
712 interquartile range. (C) Percent of miR-1 mutant animals paralyzed on plates containing 200 μM
713 aldicarb over time. Data are presented as mean ± standard deviation. (D) Percent of miR-2

714 mutant animals paralyzed on plates containing 1 mM aldicarb over time. Data are presented as
715 mean ± standard deviation. (B-D) Statistical analysis: ***p<0.001.
716
717 **Extended Data Figure 5.** Analysis of miR-58 isomiRs in miR-58 mutants. (A-B) Heatmaps
718 illustrating relative distribution of miR-58-3p (canonical guide strand) isomiRs in miR-58
719 mutants. Data are from small RNA sequencing data of L4-staged mutants that were created
720 using the (A) Nextflex v3 or (B) Nextflex v4 small RNA sequencing kits. (C-D) Heatmaps
721 illustrating relative distribution of miR-58-5p (canonical passenger strand) isomiRs in miR-58
722 mutants. Data are from small RNA sequencing data of L4-staged mutants that were created
723 using the (C) Nextflex v3 or (D) Nextflex v4 small RNA sequencing kits. (A-D) Data are
724 presented as the percent occurrence of a given isomiR within each individual mutant and do not
725 reflect possible changes in miRNA abundance. Each isomiR is illustrated on the left. The
726 maroon (guide) and gray (passenger) bars indicates the expected miR-58 sequence. Truncated
727 isomiRs are indicated by negative values corresponding to the length of the truncation.
728 Nucleotide extensions are depicted by the corresponding letters to each duplex end, which may
729 include templated or non-templated (uridylation and adenylation) extensions.
730
731 **Extended Data Figure 6.** Analysis of miR-1 and miR-2 isomiRs in miRNA mutants. Heatmaps
732 illustrate relative distribution of (A) miR-1-3p (canonical guide strand) or (B) miR-1-5p (canonical
733 passenger strand isomiRs in miR-1 mutants. (A-B) Data are from small RNA sequencing data of
734 L4-staged mutants. Heatmaps depict (C) miR-2-3p (canonical guide strand) and (D) miR-2-5p
735 (canonical passenger strand) isomiR distribution in miR-2 mutants. (C-D) Data are from small
736 RNA sequencing data of L4-staged mutants that were created using the (left) Nextflex v3 or
737 (right) Nextflex v4 small RNA sequencing kits. (A-D) Data are presented as the percent
738 occurrence of a given isomiR within each individual mutant and do not reflect possible changes
739 in miRNA abundance. Each isomiR is illustrated on the left. The maroon (guide) and gray
740 (passenger) bars indicates the expected miRNA sequence. Truncated isomiRs are indicated by
741 negative values corresponding to the length of the truncation. Nucleotide extensions are
742 depicted by the corresponding letters to each duplex end, which may include templated or non-
743 templated (uridylation and adenylation) extensions. Note that pre-miR-2 contains a templated
744 uracil immediately downstream of the 3' nucleotide of the mature miR-2 guide and passenger
745 strands, preventing disambiguation of non-templated or templated addition of uracil to either
746 strand.
747
748 **Extended Data Figure 7.** Analysis of miR-48 and miR-71 isomiRs in miRNA mutants.
749 Heatmaps illustrate relative distribution of (A) miR-48-5p (canonical guide strand), (B) miR-48-
750 3p (canonical passenger strand), (C) miR-71-5p (canonical guide strand) and (D) miR-71-3p
751 (canonical passenger strand) in miR-48 or miR-71 mutants. (A-D) Data are presented as the
752 percent occurrence of a given isomiR within each individual mutant and do not reflect possible
753 changes in miRNA abundance. Each isomiR is illustrated on the left. The maroon (guide) and
754 gray (passenger) bars indicates the expected miRNA sequence. Truncated isomiRs are
755 indicated by negative values corresponding to the length of the truncation. Nucleotide
756 extensions are depicted by the corresponding letters to each duplex end, which may include
757 templated or non-templated (uridylation and adenylation) extensions. Note that pre-miR-48
758 contains a templated adenine immediately downstream of the 3' nucleotide of the mature miR-
759 48 guide strand and a templated 3' uracil downstream immediately downstream of passenger
760 strand, preventing disambiguation of non-templated or templated additions. Similarly, pre-miR-
761 71 contains a templated uracil immediately downstream of the 3' nucleotide of the mature miR-
762 71 guide strand. (E-F) (Bottom) Schematic representations of (E) miR-48 and (F) miR-71 duplex
763 mutations that affect 3' nucleotide identity. The guide strand is shown in maroon, and the
764 passenger strand is shown in gray. The nucleotide composition of dinucleotide overhangs are

765 shown for each strand. Mutated nucleotides are indicated by red text. U:A pairs are illustrated
766 by an open circle, G:U wobble pairs are indicated by an open circle with a vertical line and G:C
767 pairs are represented by closed circles. RNAcofold was used to predict duplex structures at
768 20°C. (Top) Quantification of small RNA sequencing results for (E) miR-48 and (B) miR-71.
769 Data are presented as mean ± standard deviation, with each dot representing quantification
770 from a single library using the NEXTFLEX v4 Small RNA Sequencing Kit. Maroon bars
771 correspond to miRNA guide strands and gray bars represent miRNA passenger strands.
772 Normalization was performed by dividing raw read counts by total mapped miRNA reads and
773 multiplying by one million to acquire reads per million (rpm) values.
774
775 **Extended Data Figure 8.** The composition of dinucleotide overhangs may influence miRNA
776 strand selection. (A-B) (Left) Schematic representations of miR-58 duplex mutations that affect
777 the nucleotide composition of dinucleotide overhangs. Mutations were made in a (A) wildtype
778 miR-58 duplex background or (B) the miR-58-M7 mutant duplex. The guide strand is shown in
779 maroon, and the passenger strand is shown in gray. Mutated nucleotides are indicated by red
780 text. U:A pairs are illustrated by an open circle, G:U wobble pairs are indicated by an open circle
781 with a vertical line and G:C pairs are represented by closed circles. RNAcofold was used to
782 predict duplex structures at 20°C. (Right) Quantification of small RNA sequencing results for
783 each miR-58 duplex strand. Data are presented as mean ± standard deviation, with each dot
784 representing quantification from a single library using the NEXTFLEX v3 Small RNA
785 Sequencing Kit. Maroon bars correspond to miRNA guide strands and gray bars represent
786 miRNA passenger strands. Normalization was performed by dividing raw read counts by total
787 mapped miRNA reads and multiplying by one million to acquire reads per million (rpm) values.
788
789 **Extended Data Figure 9.** Functional analysis of ALG-1^{7A} mutants. (A) Location of alanine
790 substitutions in ALG-1^{7A} mutants. Mutations are indicated by red text. The location of the ALG-1
791 5' nucleotide binding pocket[13,14] and putative 3' nucleotide binding pocket[17] are bolded. (B)
792 Physical location of 5' nucleotide binding pocket (yellow) and putative 3' nucleotide binding
793 pocket (red) on the Alphafold predicted structure of ALG-1 (AF-Q3LTR7-F1). The MID (dark
794 purple) and PIWI (light purple) domains are marked. ChimeraX v1.9 was used for structure
795 visualization. Inset highlights relative position of the 5' nucleotide binding pocket and putative 3'
796 nucleotide binding pocket within the RNA-binding groove of ALG-1 (B') and rotated 180° (B'').
797 (C) Differential expression analysis of ALG-1^{7A} mutants compared to wildtype (N2) controls was
798 performed using the 'DESeq2' package for R. Each dot represents one miRNA strand.
799 Statistical significance was considered at $p<0.01$. Upregulated miRNAs are labelled and colored
800 pink while downregulated miRNAs are labelled and colored blue.
801
802 **Extended Data Figure 10.** Analysis of isomiRs from miRNAs transfected into human HEK293T
803 cells. Heatmaps illustrate relative distribution of (A) miR-58a-3p (*C. elegans* guide strand), (B)
804 miR-58a-5p (*C. elegans* passenger strand), (C) miR-339-syn-3p (expected guide strand) and
805 (D) miR-339-syn-5p (expected passenger strand) in miR-58 or miR-339-syn mutants. The miR-
806 339-syn mutants carry an additional internal nucleotide substitution that is not expected to
807 affected duplex structure (Supplementary Table 15), which allowed us to distinguish exogenous
808 and endogenous miR-339 variants. (A-D) Data are presented as the percent occurrence of a
809 given isomiR within each individual mutant and do not reflect possible changes in miRNA
810 abundance. Each isomiR is illustrated on the left. The maroon (guide) and gray (passenger)
811 bars indicates the expected miRNA sequence. Truncated isomiRs are indicated by negative
812 values corresponding to the length of the truncation. Nucleotide extensions are depicted by the
813 corresponding letters to each duplex end, which may include templated or non-templated
814 (uridylation and adenylation) extensions. Note that the Ultramir scaffold contains a templated

815 uracil immediately downstream of the 3' nucleotide of the 3p, preventing disambiguation of non-
816 templated or templated uridylation for the 3p strand.
817
818 **Supplementary Figure 1.** ZsGreen expression in transfected human HEK293T cells.
819 Representative images of HEK293T cells expressing ZsGreen prior to harvesting. (A) Images of
820 samples corresponding to Figure 6B. (B) Images of samples corresponding to Figure 6C.

821 **References**
822

823 1. Kim, H., Lee, Y.-Y. & Kim, V. N. The biogenesis and regulation of animal microRNAs. *Nat.*
824 *Rev. Mol. Cell Biol.* 1–21 (2024) doi:10.1038/s41580-024-00805-0.

825 2. Shang, R., Lee, S., Senavirathne, G. & Lai, E. C. microRNAs in action: biogenesis, function
826 and regulation. *Nat. Rev. Genet.* **24**, 816–833 (2023).

827 3. Denli, A. M., Tops, B. B. J., Plasterk, R. H. A., Ketting, R. F. & Hannon, G. J. Processing of
828 primary microRNAs by the Microprocessor complex. *Nature* **432**, 231–235 (2004).

829 4. Gregory, R. I. *et al.* The Microprocessor complex mediates the genesis of microRNAs. *Nature*
830 **432**, 235–240 (2004).

831 5. Lee, Y., Jeon, K., Lee, J., Kim, S. & Kim, V. N. MicroRNA maturation: stepwise processing
832 and subcellular localization. *EMBO J.* **21**, 4663–4670 (2002).

833 6. Lee, Y. *et al.* The nuclear RNase III Drosha initiates microRNA processing. *Nature* **425**, 415–
834 419 (2003).

835 7. Grishok, A. *et al.* Genes and Mechanisms Related to RNA Interference Regulate Expression
836 of the Small Temporal RNAs that Control C. elegans Developmental Timing. *Cell* **106**, 23–34
837 (2001).

838 8. Hutvágner, G. *et al.* A Cellular Function for the RNA-Interference Enzyme Dicer in the
839 Maturation of the let-7 Small Temporal RNA. *Science* **293**, 834–838 (2001).

840 9. Jiang, F. *et al.* Dicer-1 and R3D1-L catalyze microRNA maturation in Drosophila. *Genes Dev.*
841 **19**, 1674–1679 (2005).

842 10. Ketting, R. F. *et al.* Dicer functions in RNA interference and in synthesis of small RNA
843 involved in developmental timing in C. elegans. *Genes Dev.* **15**, 2654–2659 (2001).

844 11. Knight, S. W. & Bass, B. L. A Role for the RNase III Enzyme DCR-1 in RNA Interference
845 and Germ Line Development in Caenorhabditis elegans. *Science* **293**, 2269–2271 (2001).

846 12. Saito, K., Ishizuka, A., Siomi, H. & Siomi, M. C. Processing of Pre-microRNAs by the Dicer-
847 1–Loquacious Complex in Drosophila Cells. *PLoS Biol.* **3**, e235 (2005).

848 13. Elkayam, E. *et al.* The Structure of Human Argonaute-2 in Complex with miR-20a. *Cell* **150**,
849 100–110 (2012).

850 14. Schirle, N. T. & MacRae, I. J. The Crystal Structure of Human Argonaute2. *Science* **336**,
851 1037–1040 (2012).

852 15. Nykänen, A., Haley, B. & Zamore, P. D. ATP Requirements and Small Interfering RNA
853 Structure in the RNA Interference Pathway. *Cell* **107**, 309–321 (2001).

854 16. Schwarz, D. S. *et al.* Asymmetry in the Assembly of the RNAi Enzyme Complex. *Cell* **115**,
855 199–208 (2003).

856 17. Suzuki, H. I. *et al.* Small-RNA asymmetry is directly driven by mammalian Argonautes. *Nat*
857 *Struct Mol Biol* **22**, 512–521 (2015).

858 18. Medley, J. C., Panzade, G. & Zinovyeva, A. Y. microRNA strand selection: Unwinding the
859 rules. *Wiley Interdiscip. Rev.: RNA* **12**, e1627 (2021).

860 19. Humphreys, D. T. *et al.* Complexity of Murine Cardiomyocyte miRNA Biogenesis, Sequence
861 Variant Expression and Function. *PLoS ONE* **7**, e30933 (2012).

862 20. Okamura, K. *et al.* The regulatory activity of microRNA* species has substantial influence on
863 microRNA and 3′ UTR evolution. *Nat. Struct. Mol. Biol.* **15**, 354–363 (2008).

864 21. Ghildiyal, M., Xu, J., Seitz, H., Weng, Z. & Zamore, P. D. Sorting of Drosophila small
865 silencing RNAs partitions microRNA* strands into the RNA interference pathway. *RNA* **16**, 43–
866 56 (2010).

867 22. Kuchen, S. *et al.* Regulation of MicroRNA Expression and Abundance during
868 Lymphopoiesis. *Immunity* **32**, 828–839 (2010).

869 23. Ro, S., Park, C., Young, D., Sanders, K. M. & Yan, W. Tissue-dependent paired expression
870 of miRNAs. *Nucleic Acids Res.* **35**, 5944–5953 (2007).

871 24. Yang, J.-S. *et al.* Widespread regulatory activity of vertebrate microRNA* species. *RNA* **17**,
872 312–326 (2011).

873 25. Frank, F., Sonenberg, N. & Nagar, B. Structural basis for 5′-nucleotide base-specific
874 recognition of guide RNA by human AGO2. *Nature* **465**, 818–822 (2010).

875 26. Khvorova, A., Reynolds, A. & Jayasena, S. D. Functional siRNAs and miRNAs Exhibit
876 Strand Bias. *Cell* **115**, 209–216 (2003).

877 27. Warf, M. B., Johnson, W. E. & Bass, B. L. Improved annotation of C. elegans microRNAs by
878 deep sequencing reveals structures associated with processing by Drosha and Dicer. *RNA* **17**,
879 563–577 (2011).

880 28. Medley, J. C. & Zinovyeva, A. In silico unwinding of Caenorhabditis elegans microRNA
881 duplexes to evaluate thermodynamic end stabilities improves predictions of microRNA strand
882 selection. *bioRxiv* 2025.06.26.661848 (2025) doi:10.1101/2025.06.26.661848.

883 29. Panzade, G., Li, L., Hebbar, S., Veksler-Lublinsky, I. & Zinovyeva, A. Global profiling and
884 annotation of templated isomiRs dynamics across Caenorhabditis elegans development. *RNA*
885 *Biol.* **19**, 928–942 (2022).

886 30. Alvarez-Saavedra, E. & Horvitz, H. R. Many Families of C. elegans MicroRNAs Are Not
887 Essential for Development or Viability. *Curr Biol* **20**, 367–373 (2010).

888 31. Simon, D. J. *et al.* The MicroRNA miR-1 Regulates a MEF-2-Dependent Retrograde Signal
889 at Neuromuscular Junctions. *Cell* **133**, 903–915 (2008).

890 32. O'Hern, P. J. *et al.* Decreased microRNA levels lead to deleterious increases in neuronal M2
891 muscarinic receptors in Spinal Muscular Atrophy models. *eLife* **6**, e20752 (2017).

892 33. Lingel, A., Simon, B., Izaurralde, E. & Sattler, M. Nucleic acid 3′-end recognition by the
893 Argonaute2 PAZ domain. *Nat. Struct. Mol. Biol.* **11**, 576–577 (2004).

894 34. Wang, Y., Sheng, G., Juranek, S., Tuschl, T. & Patel, D. J. Structure of the guide-strand-
895 containing argonaute silencing complex. *Nature* **456**, 209–13 (2008).

896 35. Ameres, S. L. & Zamore, P. D. Diversifying microRNA sequence and function. *Nat. Rev.*
897 *Mol. Cell Biol.* **14**, 475–488 (2013).

898 36. Han, J. & Mendell, J. T. MicroRNA turnover: a tale of tailing, trimming, and targets. *Trends*
899 *Biochem. Sci.* **48**, 26–39 (2023).

900 37. Kozomara, A., Birgaoanu, M. & Griffiths-Jones, S. miRBase: from microRNA sequences to
901 function. *Nucleic Acids Res.* **47**, D155–D162 (2018).

902 38. Creugny, A., Fender, A. & Pfeffer, S. Regulation of primary microRNA processing. *FEBS*
903 *Lett.* **592**, 1980–1996 (2018).

904 39. Han, J. *et al.* The Drosha-DGCR8 complex in primary microRNA processing. *Genes Dev.*
905 **18**, 3016–3027 (2004).

906 40. Knott, S. R. V. *et al.* A Computational Algorithm to Predict shRNA Potency. *Mol. Cell* **56**,
907 796–807 (2014).

908 41. Newman, M. A., Mani, V. & Hammond, S. M. Deep sequencing of microRNA precursors
909 reveals extensive 3′ end modification. *RNA* **17**, 1795–1803 (2011).

910 42. Wyman, S. K. *et al.* Post-transcriptional generation of miRNA variants by multiple nucleotidyl
911 transferases contributes to miRNA transcriptome complexity. *Genome Res* **21**, 1450–61 (2011).

912 43. Fernández-Pérez, D., Brieño-Enríquez, M. A., Isoler-Alcaraz, J., Larriba, E. & Mazo, J. del.
913 MicroRNA dynamics at the onset of primordial germ and somatic cell sex differentiation during
914 mouse embryonic gonad development. *Rna* **24**, 287–303 (2018).

915 44. Fernandez-Valverde, S. L., Taft, R. J. & Mattick, J. S. Dynamic isomiR regulation in
916 Drosophila development. *RNA* **16**, 1881–1888 (2010).

917 45. Oliveira, A. C. de *et al.* MicroRNA Transcriptomes Reveal Prevalence of Rare and Species-
918 Specific Arm Switching Events During Zebrafish Ontogenesis. *Evol. Bioinform. Online* **20**,
919 11769343241263230 (2024).

920 46. Londin, E. *et al.* Analysis of 13 cell types reveals evidence for the expression of numerous
921 novel primate- and tissue-specific microRNAs. *Proc. Natl. Acad. Sci.* **112**, E1106–E1115 (2015).

922 47. Smith, C. M. & Hutvagner, G. A comparative analysis of single cell small RNA sequencing
923 data reveals heterogeneous isomiR expression and regulation. *Sci. Rep.* **12**, 2834 (2022).

924 48. Telonis, A. G. *et al.* Knowledge about the presence or absence of miRNA isoforms
925 (isomiRs) can successfully discriminate amongst 32 TCGA cancer types. *Nucleic Acids Res.* **45**,
926 2973–2985 (2017).

927 49. Vieux, K.-F. *et al.* Screening by deep sequencing reveals mediators of microRNA tailing in
928 C. elegans. *Nucleic Acids Res* **49**, gkab840- (2021).

929 50. Burroughs, A. M. *et al.* A comprehensive survey of 3′ animal miRNA modification events and
930 a possible role for 3′ adenylation in modulating miRNA targeting effectiveness. *Genome Res.*
931 **20**, 1398–1410 (2010).

932 51. Heo, I. *et al.* Lin28 Mediates the Terminal Uridylation of let-7 Precursor MicroRNA. *Mol. Cell*
933 **32**, 276–284 (2008).

934 52. Heo, I. *et al.* Mono-Uridylation of Pre-MicroRNA as a Key Step in the Biogenesis of Group II
935 let-7 MicroRNAs. *Cell* **151**, 521–532 (2012).

936 53. Kim, H. *et al.* A Mechanism for microRNA Arm Switching Regulated by Uridylation. *Mol Cell*
937 **78**, 1224-1236.e5 (2020).

938 54. Song, J. *et al.* Prevalent cytidylation and uridylation of precursor miRNAs in Arabidopsis.
939 *Nat. Plants* **5**, 1260–1272 (2019).

940 55. Kwak, P. B. & Tomari, Y. The N domain of Argonaute drives duplex unwinding during RISC
941 assembly. *Nat Struct Mol Biol* **19**, 145–151 (2012).

942 56. Duan, Y. *et al.* Modeling neurodevelopmental disorder-associated human AGO1 mutations
943 in Caenorhabditis elegans Argonaute alg-1. *Proc. Natl. Acad. Sci.* **121**, e2308255121 (2024).

944 57. Zinovyeva, A. Y., Veksler-Lublinsky, I., Vashisht, A. A., Wohlschlegel, J. A. & Ambros, V. R.
945 Caenorhabditis elegans ALG-1 antimorphic mutations uncover functions for Argonaute in
946 microRNA guide strand selection and passenger strand disposal. *Proc. Natl. Acad. Sci.* **112**,
947 E5271–E5280 (2015).

948 58. Kim, Y. *et al.* Deletion of human tarbp2 reveals cellular microRNA targets and cell-cycle
949 function of TRBP. *Cell Reports* **9**, 1061–74 (2014).

950 59. Noland, C. L. & Doudna, J. A. Multiple sensors ensure guide strand selection in human
951 RNAi pathways. *RNA* **19**, 639–648 (2013).

952 60. Wilson, R. C. *et al.* Dicer-TRBP Complex Formation Ensures Accurate Mammalian
953 MicroRNA Biogenesis. *Mol. Cell* **57**, 397–407 (2015).

954 61. Brenner, S. The Genetics of Caenorhabditis elegans. *Genetics* **77**, 71–94 (1974).

955 62. Hibshman, J. D., Webster, A. K. & Baugh, L. R. Liquid-culture protocols for synchronous
956 starvation, growth, dauer formation, and dietary restriction of Caenorhabditis elegans. *STAR*
957 *Protoc.* **2**, 100276 (2021).

958 63. Porta-de-la-Riva, M., Fontrodona, L., Villanueva, A. & Cerón, J. Basic Caenorhabditis
959 elegans methods: synchronization and observation. *J. Vis. Exp. : JoVE* e4019 (2012)
960 doi:10.3791/4019.

961 64. Lorenz, R. *et al.* ViennaRNA Package 2.0. *Algorithms Mol. Biol. : AMB* **6**, 26 (2011).

962 65. Paix, A., Folkmann, A., Rasoloson, D. & Seydoux, G. High Efficiency, Homology-Directed
963 Genome Editing in Caenorhabditis elegans Using CRISPR-Cas9 Ribonucleoprotein Complexes.
964 *Genetics* **201**, 47–54 (2015).

965 66. Martin, M. Cutadapt removes adapter sequences from high-throughput sequencing reads.
966 *EMBnetJ.* **17**, 10–12 (2011).

967 67. Andrews. FastQC: A Quality Control Tool for High Throughput Sequence Data. *Available*
968 *online at: http://www.bioinformatics.babraham.ac.uk/projects/fastqc/* (2010).

969 68. Langmead, B., Trapnell, C., Pop, M. & Salzberg, S. L. Ultrafast and memory-efficient
970 alignment of short DNA sequences to the human genome. *Genome Biol.* **10**, R25–R25 (2009).

971 69. Li, H. *et al.* The Sequence Alignment/Map format and SAMtools. *Bioinformatics* **25**, 2078–
972 2079 (2009).

973 70. Donnelly, B. F. *et al.* The developmentally timed decay of an essential microRNA family is
974 seed-sequence dependent. *Cell Rep.* **40**, 111154–111154 (2022).

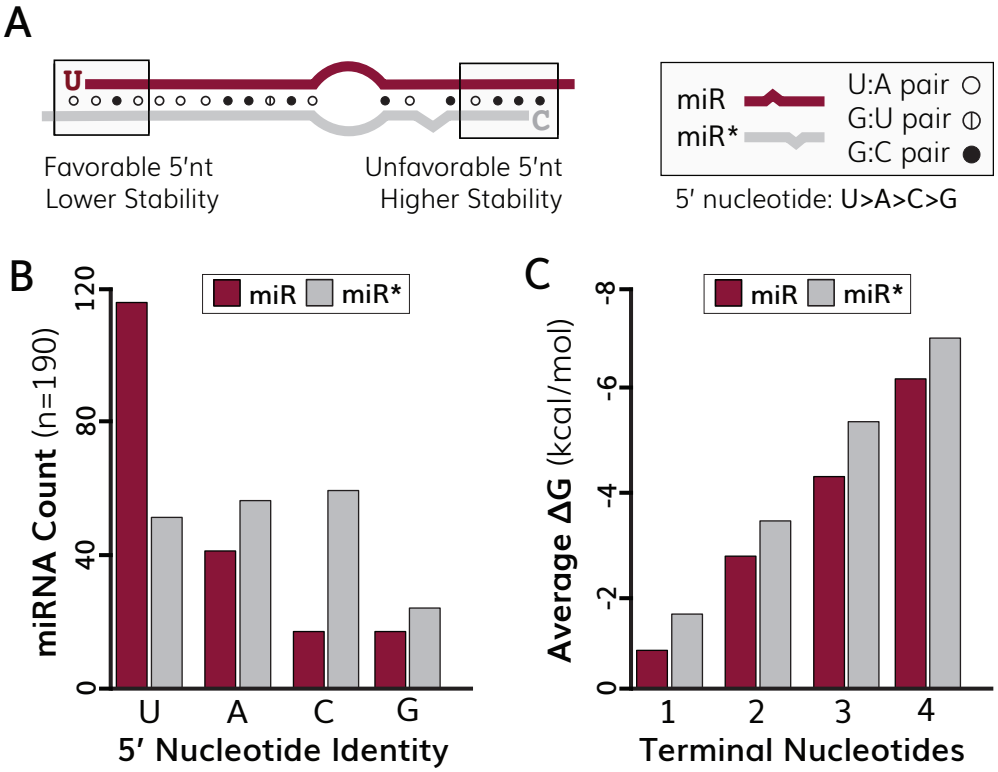
A
U
C
Favorable 5′nt
Lower Stability
Unfavorable 5′nt
Higher Stability
miR
miR*
U:A pair
G:U pair
G:C pair
5′ nucleotide: U>A>C>G
B
miR
miR*
miRNA Count (n=190)
0
40
80
120
U
A
C
G
5′ Nucleotide Identity
C
miR
miR*
Average ΔG (kcal/mol)
0
-2
-4
-6
-8
1
2
3
4
Terminal Nucleotides

Figure 1

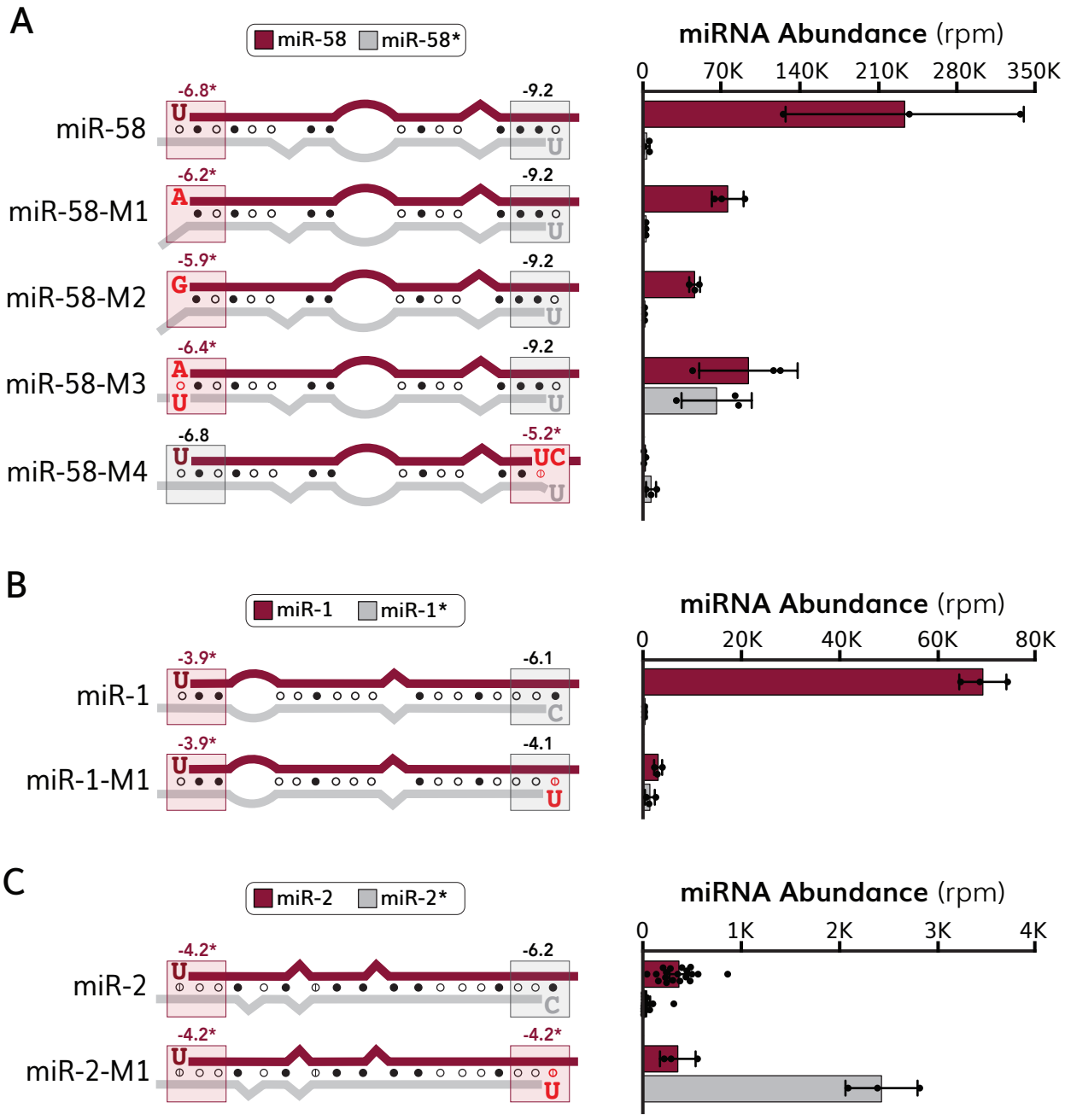
A
miR-58
miR-58*
miRNA Abundance (rpm)
0
70K
140K
210K
280K
350K
miR-58
miR-58-M1
miR-58-M2
miR-58-M3
miR-58-M4
-6.8*
-9.2
-6.2*
-5.9*
-6.4*
-6.8
-5.2*
B
miR-1
miR-1*
0
20K
40K
60K
80K
miR-1
miR-1-M1
-3.9*
-6.1
-4.1
C
miR-2
miR-2*
0
1K
2K
3K
4K
miR-2
miR-2-M1
-4.2*
-6.2

Figure 2

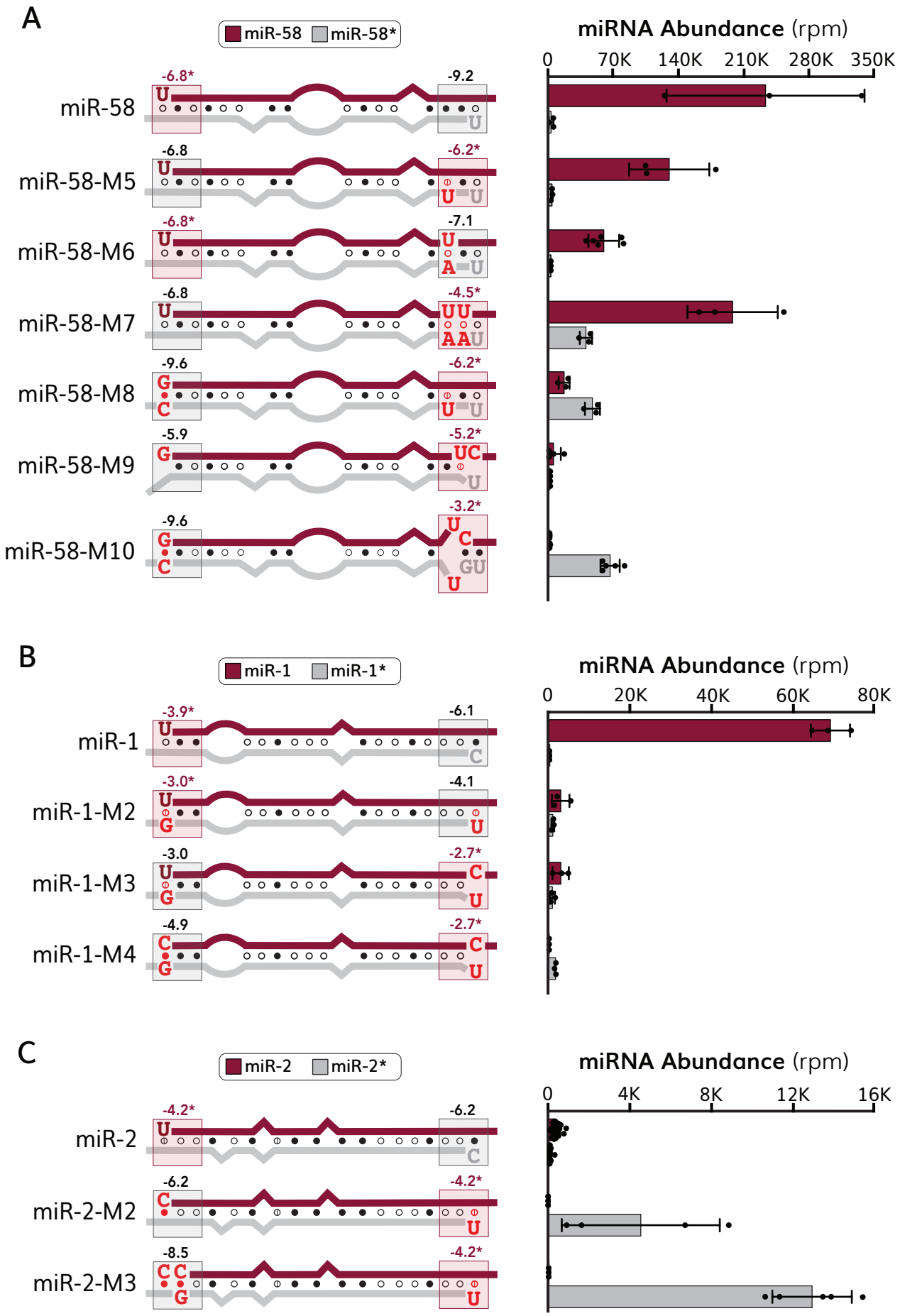
A
miR-58
miR-58*
miRNA Abundance (rpm)
0
70K
140K
210K
280K
350K
miR-58
miR-58-M5
miR-58-M6
miR-58-M7
miR-58-M8
miR-58-M9
miR-58-M10
-6.8*
-9.2
-6.8
-6.2*
-6.8*
-7.1
-6.8
-4.5*
-9.6
-6.2*
-5.9
-5.2*
-9.6
-3.2*
B
miR-1
miR-1*
miRNA Abundance (rpm)
0
20K
40K
60K
80K
miR-1
miR-1-M2
miR-1-M3
miR-1-M4
-3.9*
-6.1
-3.0*
-4.1
-3.0
-2.7*
-4.9
-2.7*
C
miR-2
miR-2*
miRNA Abundance (rpm)
0
4K
8K
12K
16K
miR-2
miR-2-M2
miR-2-M3
-4.2*
-6.2
-6.2
-4.2*
-8.5
-4.2*

Figure 3

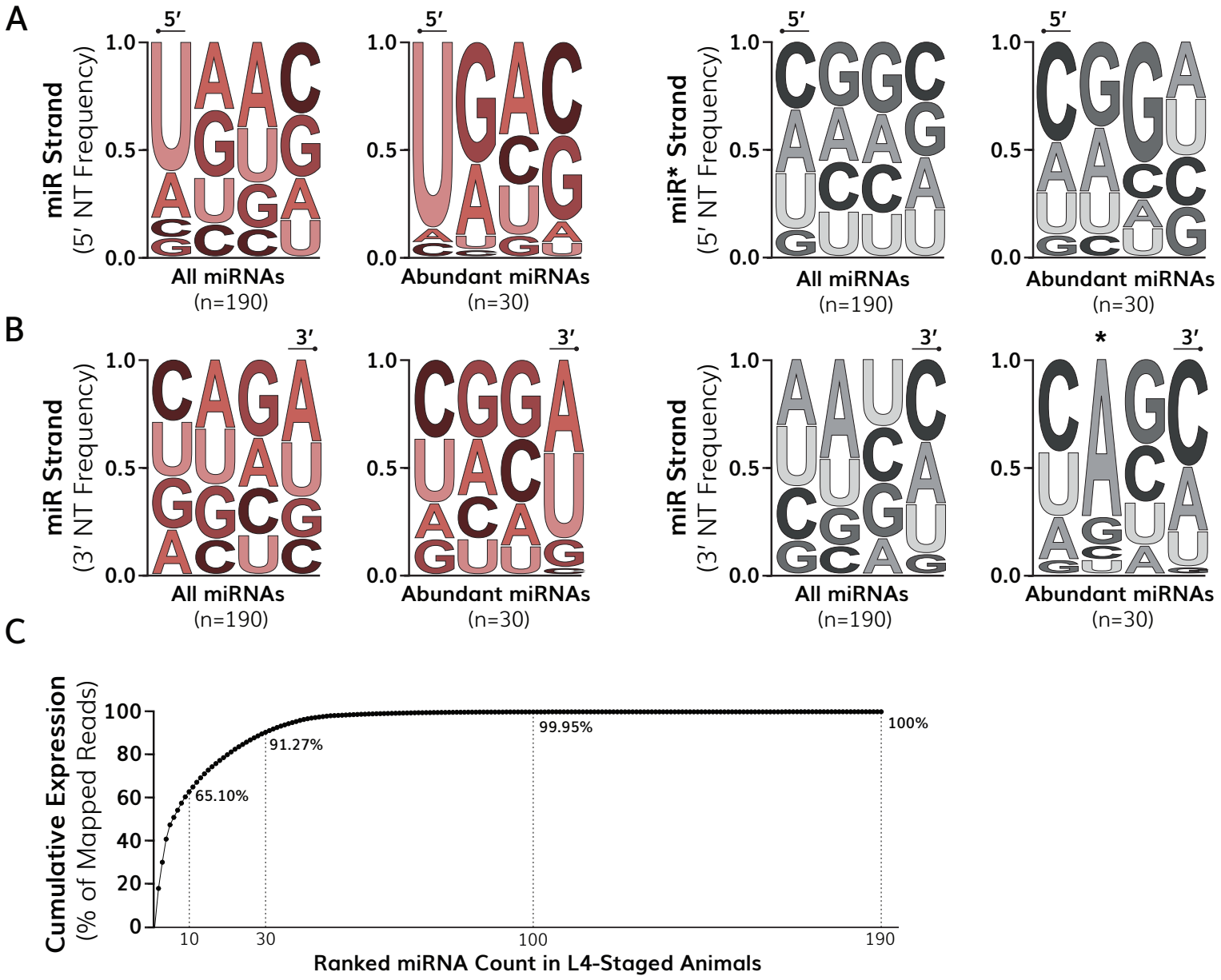
A
5′
miR Strand
(5′ NT Frequency)
1.0
0.5
0.0
All miRNAs
(n=190)
Abundant miRNAs
(n=30)
miR* Strand
B
3′
*
C
Cumulative Expression
(% of Mapped Reads)
100
80
60
40
20
0
65.10%
91.27%
99.95%
100%
10
30
100
190
Ranked miRNA Count in L4-Staged Animals

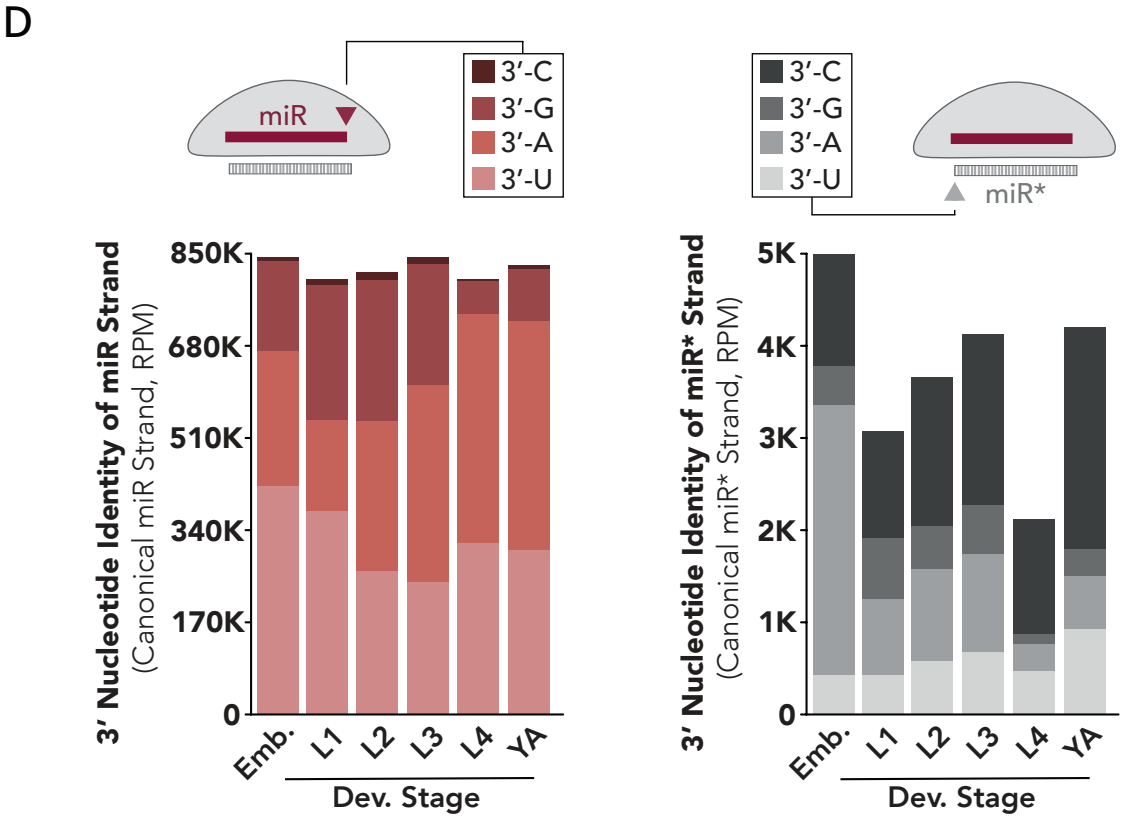
D
miR
miR*
3′-C
3′-G
3′-A
3′-U
3′ Nucleotide Identity of miR Strand
(Canonical miR Strand, RPM)
850K
680K
510K
340K
170K
0
3′ Nucleotide Identity of miR* Strand
(Canonical miR* Strand, RPM)
5K
4K
3K
2K
1K
Emb.
L1
L2
L3
L4
YA
Dev. Stage

Figure 4

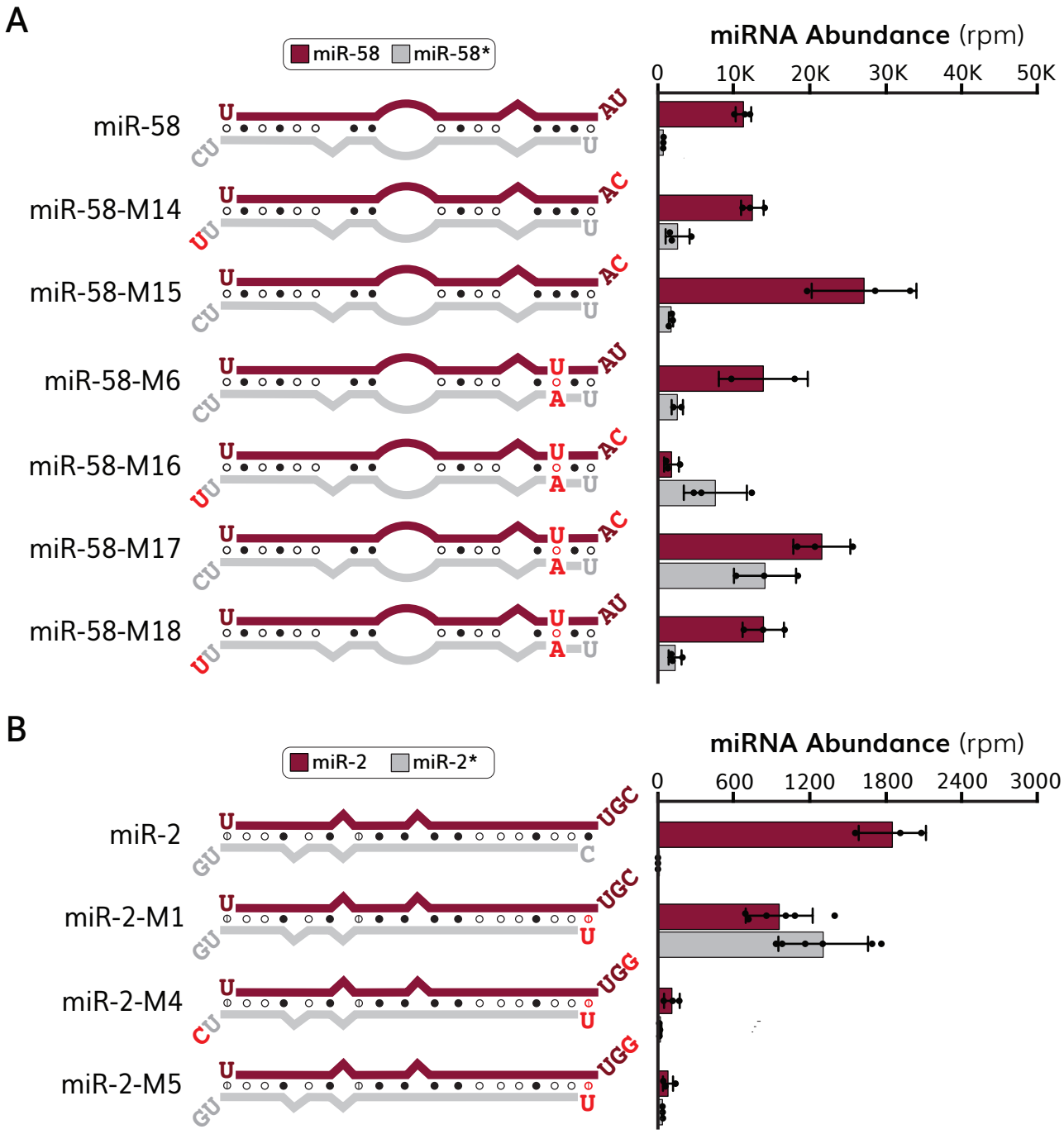
A
miR-58
miR-58*
miRNA Abundance (rpm)
0
10K
20K
30K
40K
50K
miR-58
miR-58-M14
miR-58-M15
miR-58-M6
miR-58-M16
miR-58-M17
miR-58-M18
B
miR-2
miR-2*
miRNA Abundance (rpm)
0
600
1200
1800
2400
3000
miR-2
miR-2-M1
miR-2-M4
miR-2-M5

Figure 5

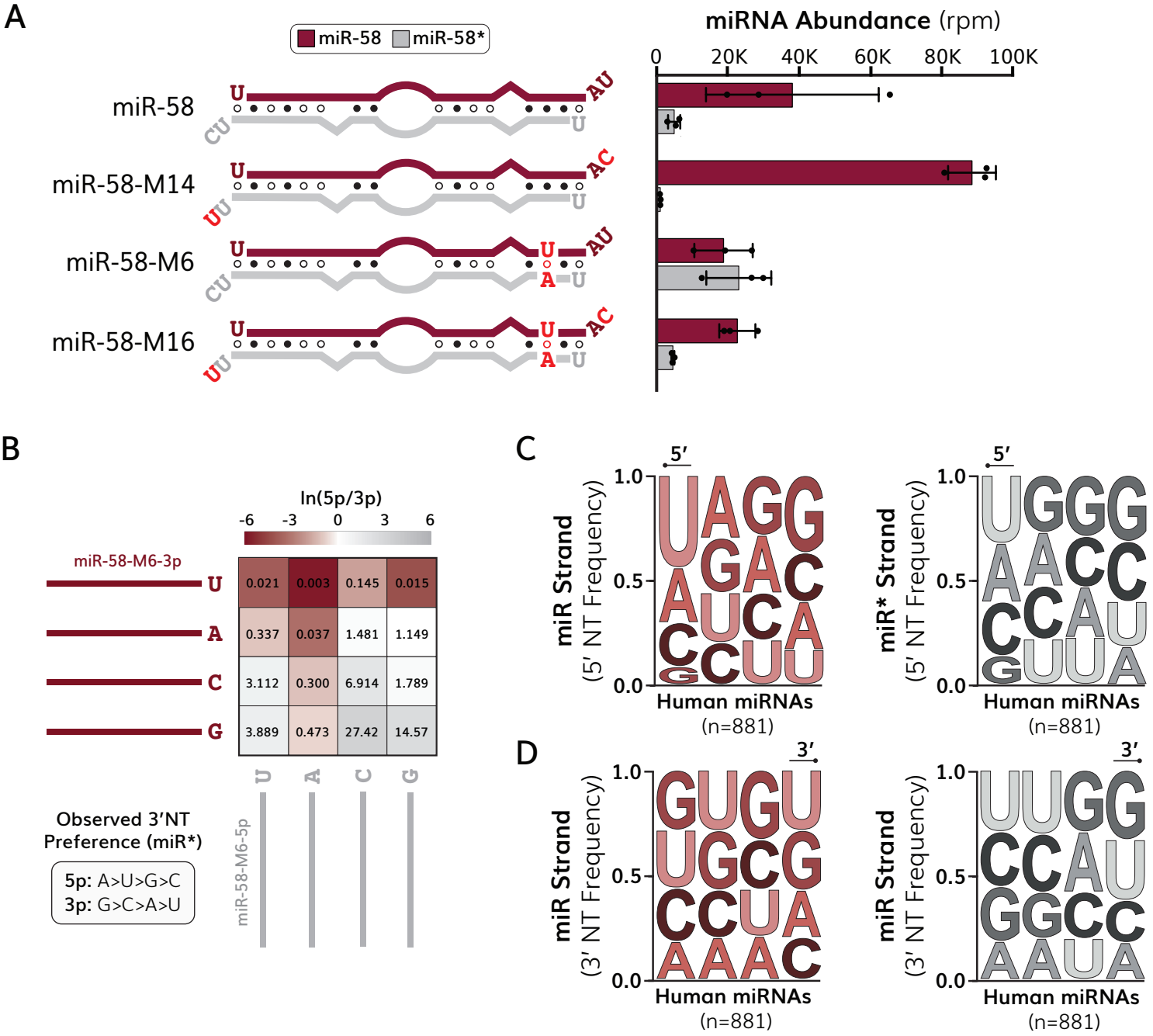
A
miR-58
miR-58*
miR-58
miR-58-M14
miR-58-M6
miR-58-M16
miRNA Abundance (rpm)
0
20K
40K
60K
80K
100K
B
ln(5p/3p)
-6
-3
0
3
6
miR-58-M6-3p
U
A
C
G
0.021
0.003
0.145
0.015
0.337
0.037
1.481
1.149
3.112
0.300
6.914
1.789
3.889
0.473
27.42
14.57
miR-58-M6-5p
Observed 3'NT Preference (miR*)
5p: A>U>G>C
3p: G>C>A>U
C
5'
miR Strand
(5' NT Frequency)
miR* Strand
(5' NT Frequency)
Human miRNAs
(n=881)
D
3'
(3' NT Frequency)
1.0
0.5
0.0

E

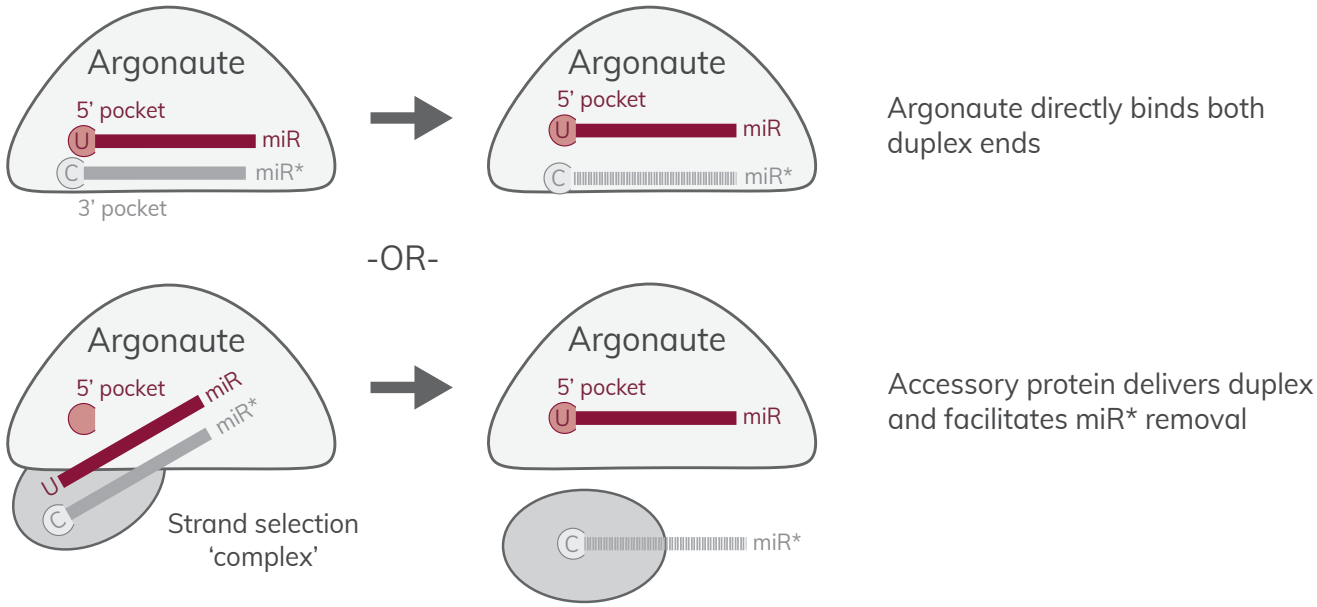
Argonaute
5' pocket
miR
miR*
3' pocket
Argonaute directly binds both duplex ends
-OR-
Strand selection 'complex'
Accessory protein delivers duplex and facilitates miR* removal

Figure 6

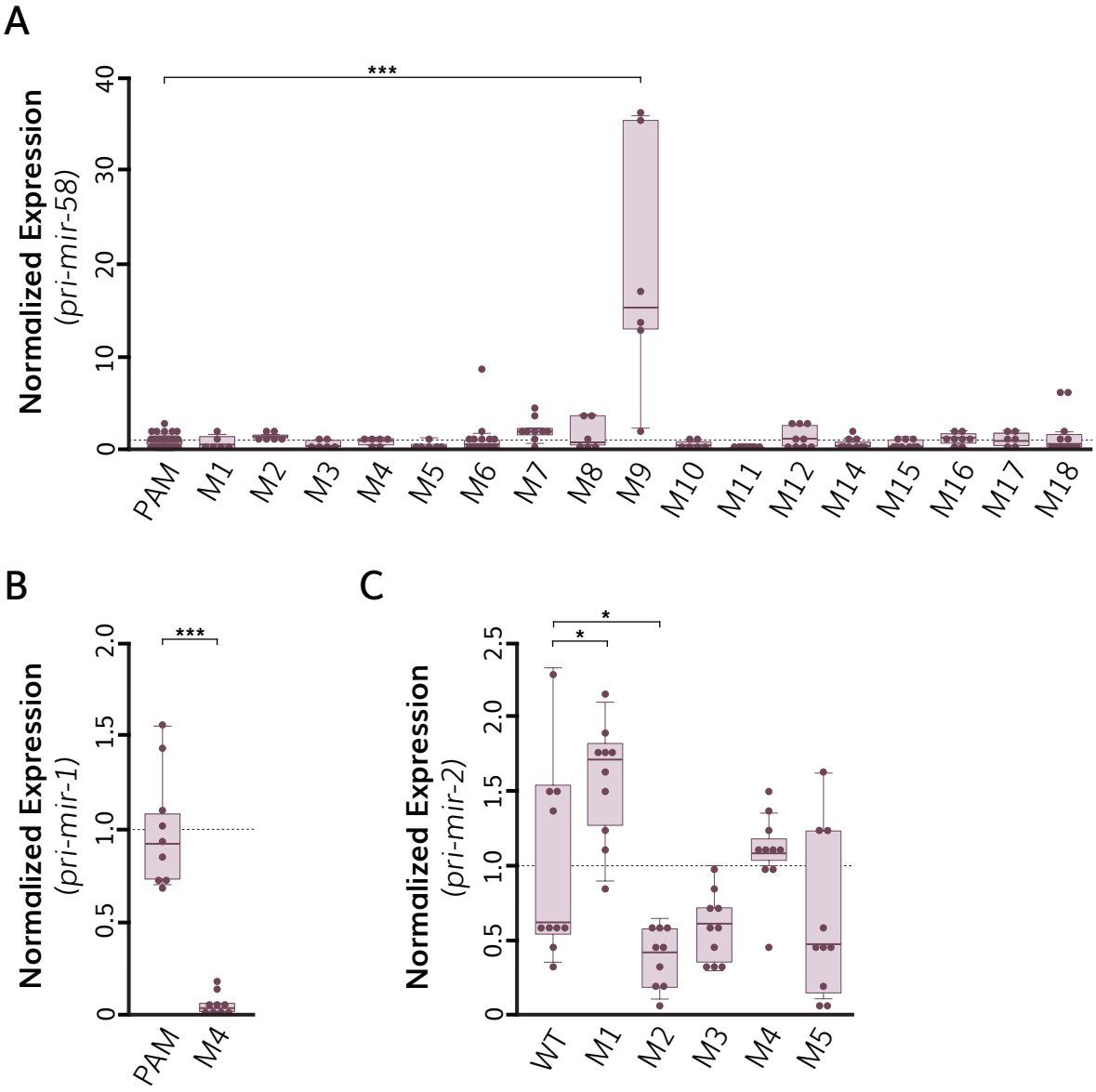

Extended Data Figure 1

A

	Seed
miR-58	UGAGAUCGUUCAGUACGGCAAU
miR-80	UGAGAUCAUUAGUUGAAAGCCGA
miR-81	UGAGAUCAUCGUGAAAGCUAGU
miR-82	UGAGAUCAUCGUGAAAGCCAGU

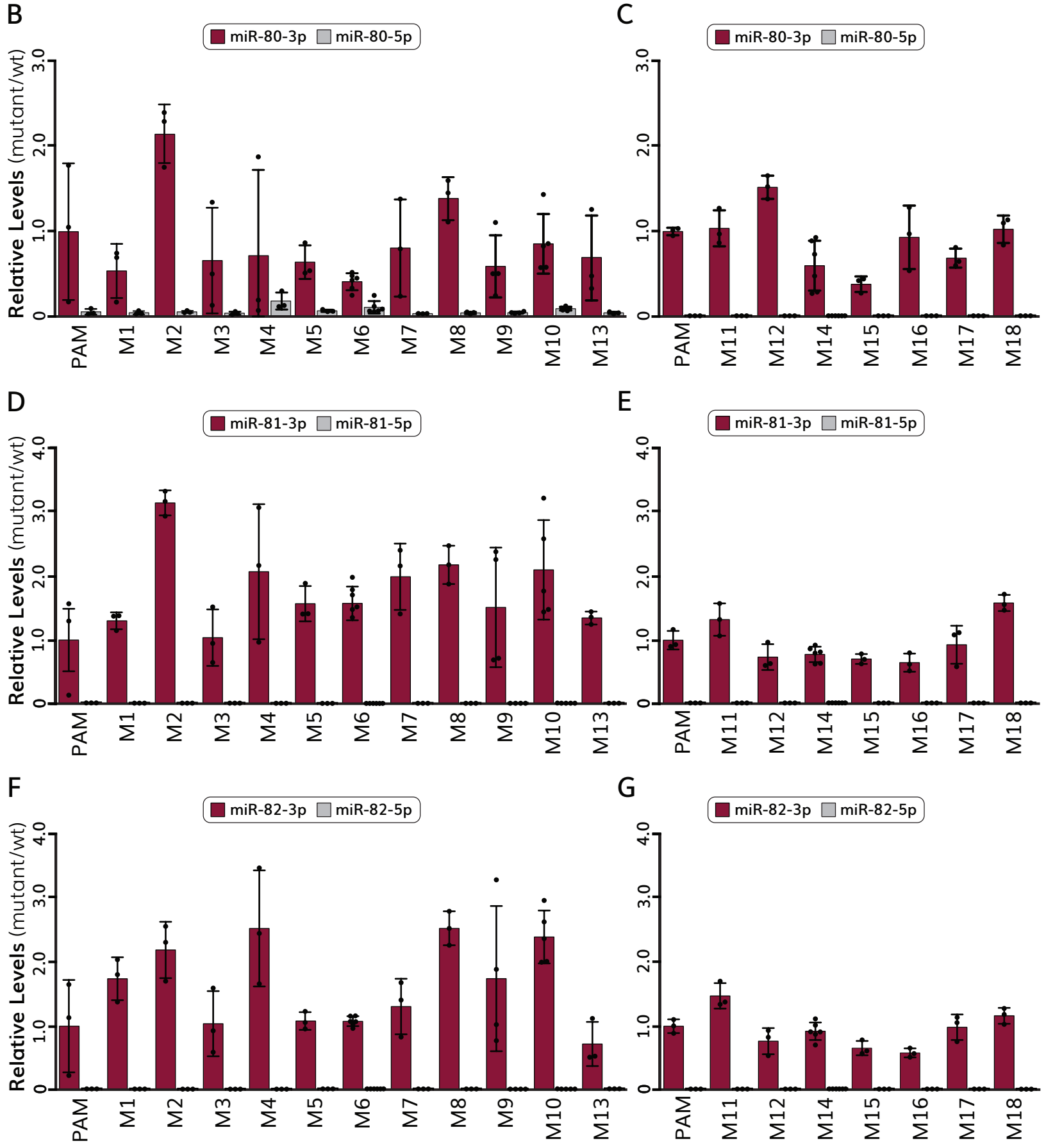

Extended Data Figure 2

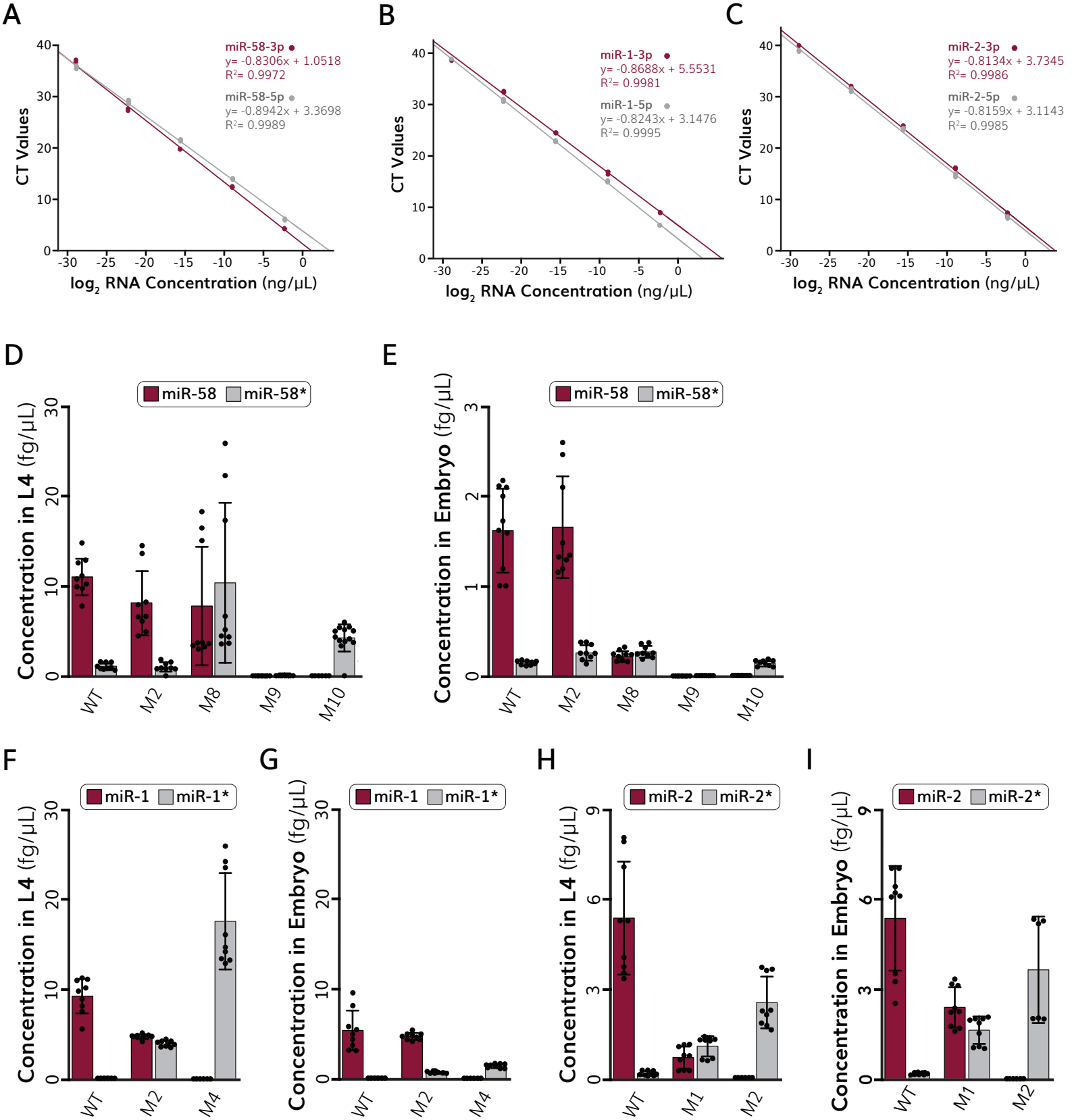

Extended Data Figure 3

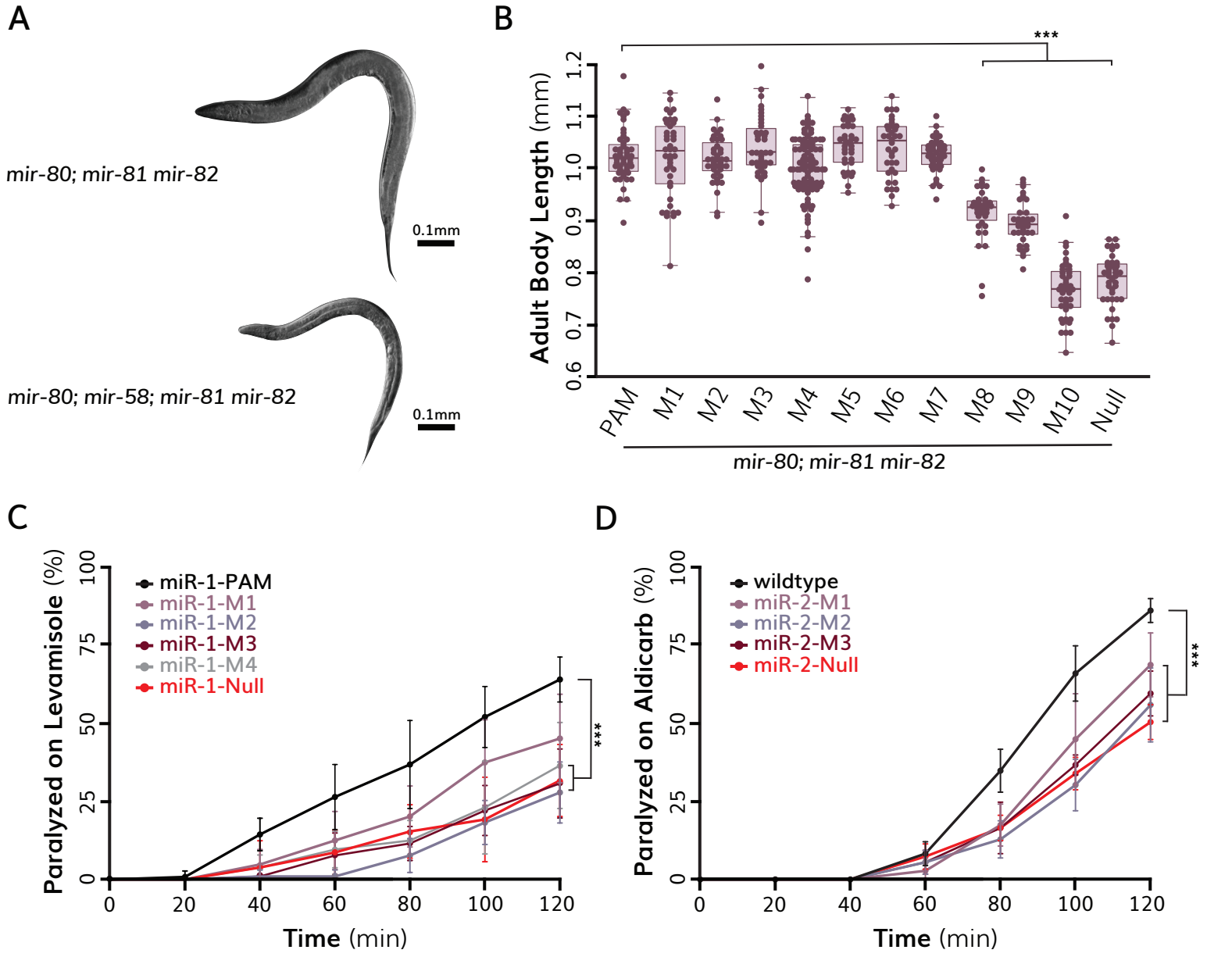

Extended Data Figure 4

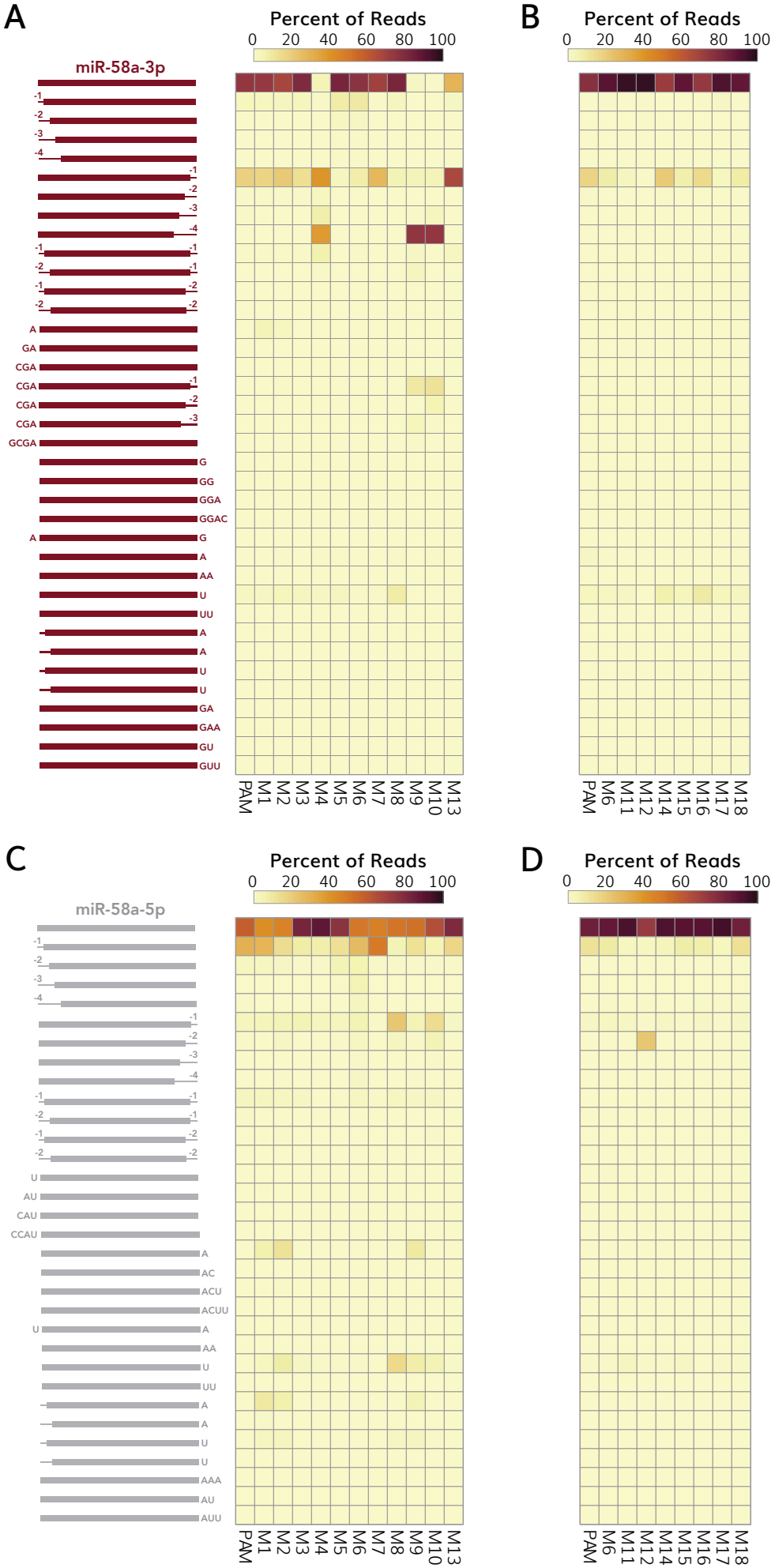

Extended Data Figure 5

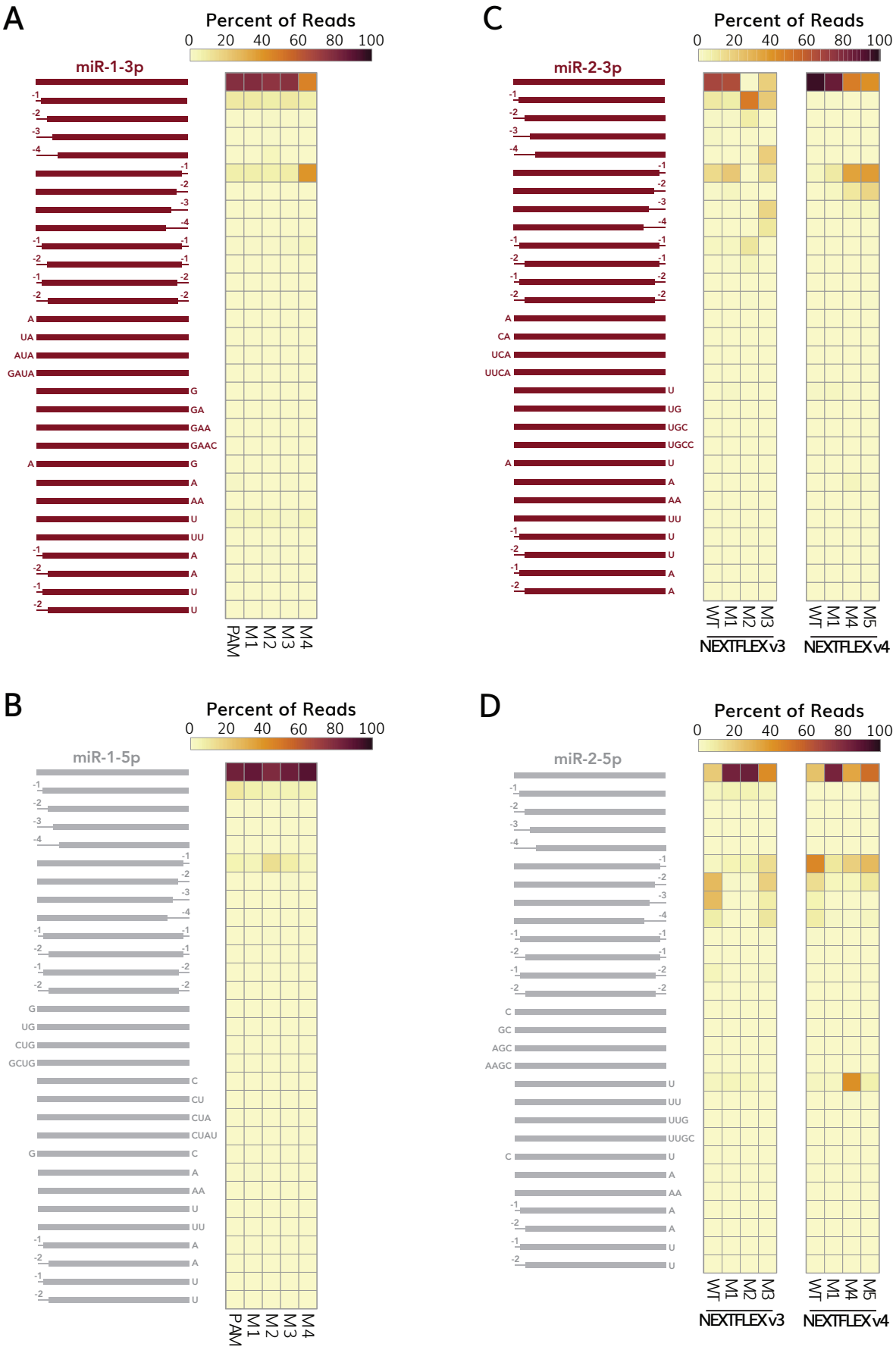

Extended Data Figure 6

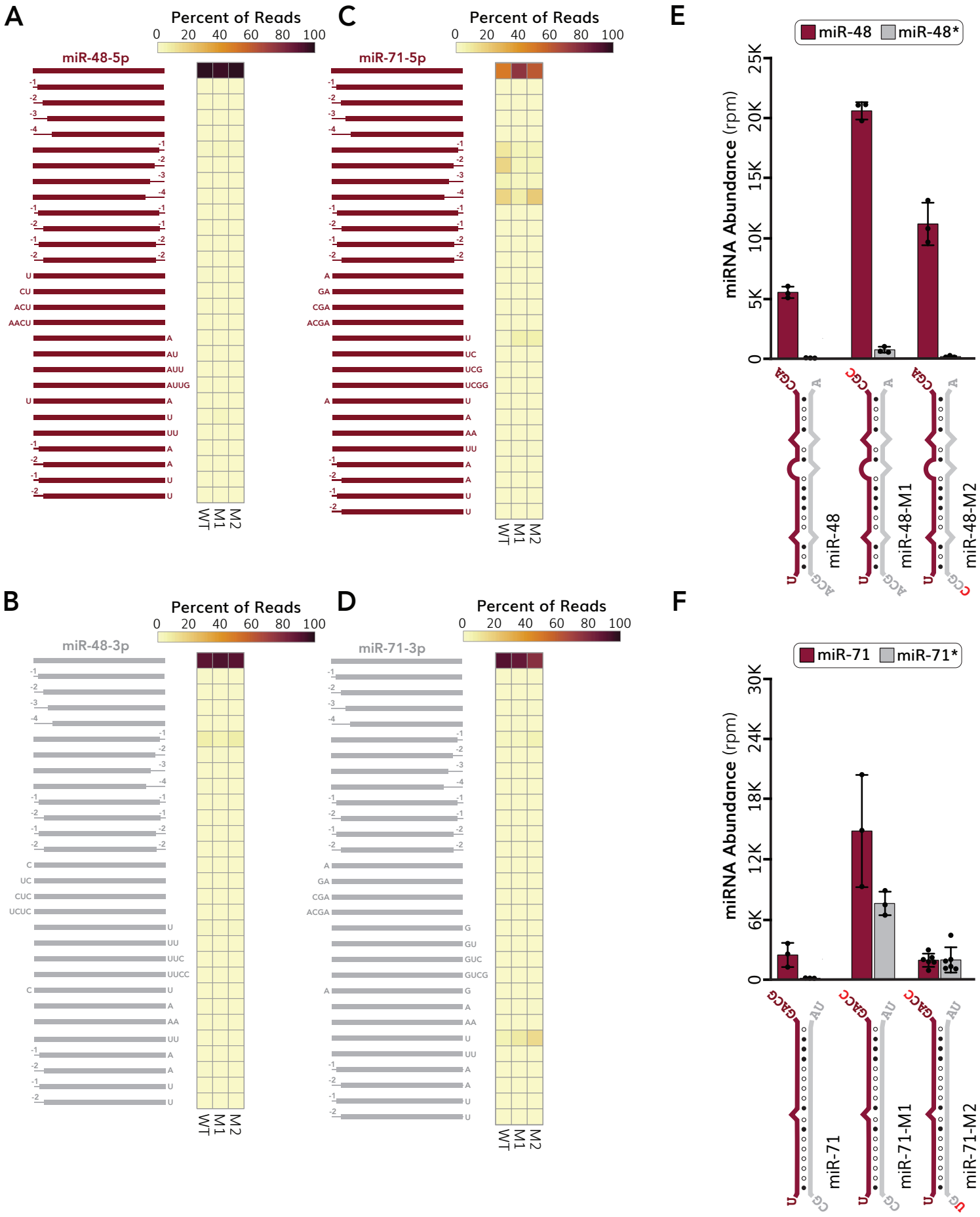

Extended Data Figure 7

A

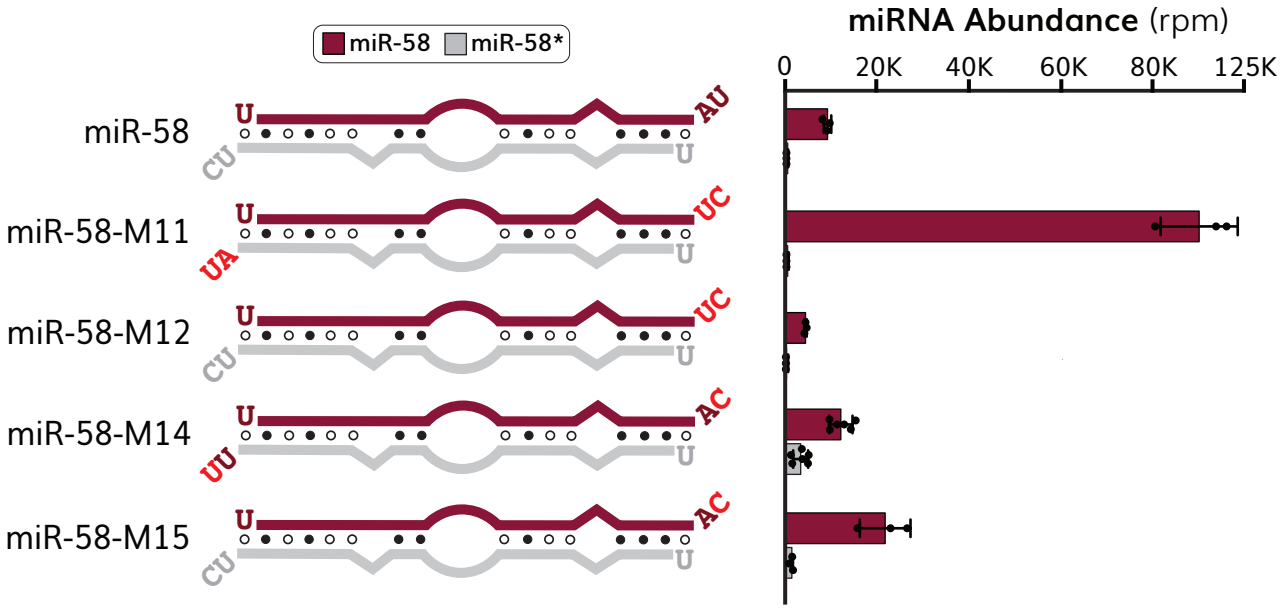

B

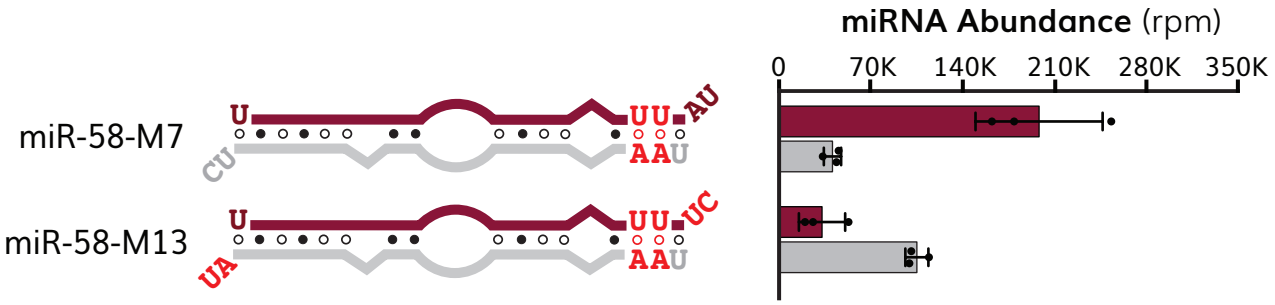

Extended Data Figure 8

A

5′ nt (guide) 3′ nt (passenger)

ALG-1 PMFKYLKQNYSGIQLVVVVL**PGKTP**VYAEVKRVGDTVLGIATQCVQAKNAI**RTTPQTL**SNLCLKMNVKLGGVNSI - 720

ALG-1^{7A} PMFKYLKQNYSGIQLVVVVL**PGKTP**VYAEVKRVGDTVLGIATQCVQAKNAI**AAAAAAA**SNLCLKMNVKLGGVNSI - 720

ALG-1^{7A}: R697A, T698A, T699A, P700A, Q701A, T702A, L703A

B **ALG-1** (AF-Q3LTR7-F1)

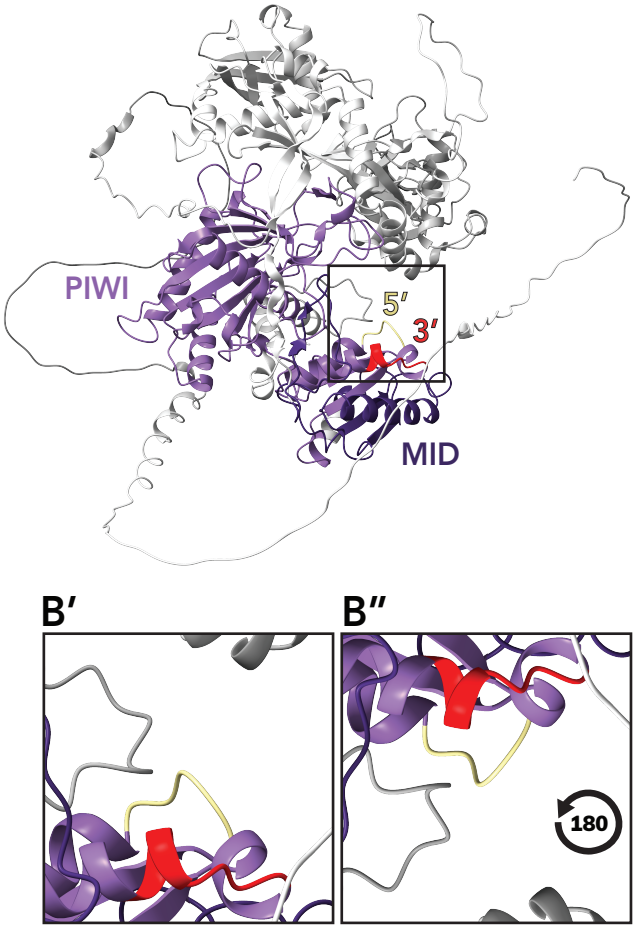

C

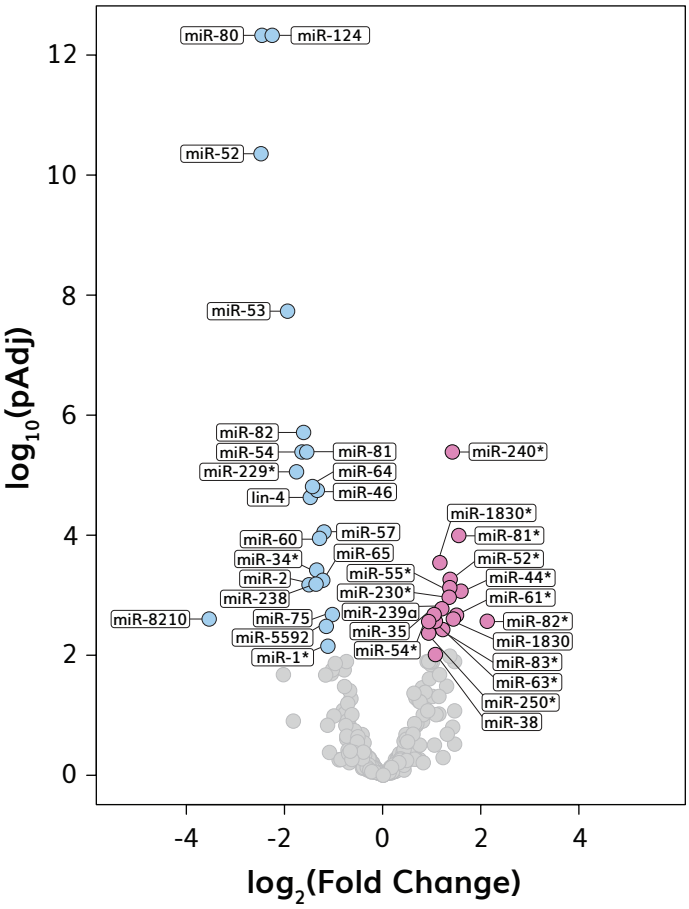

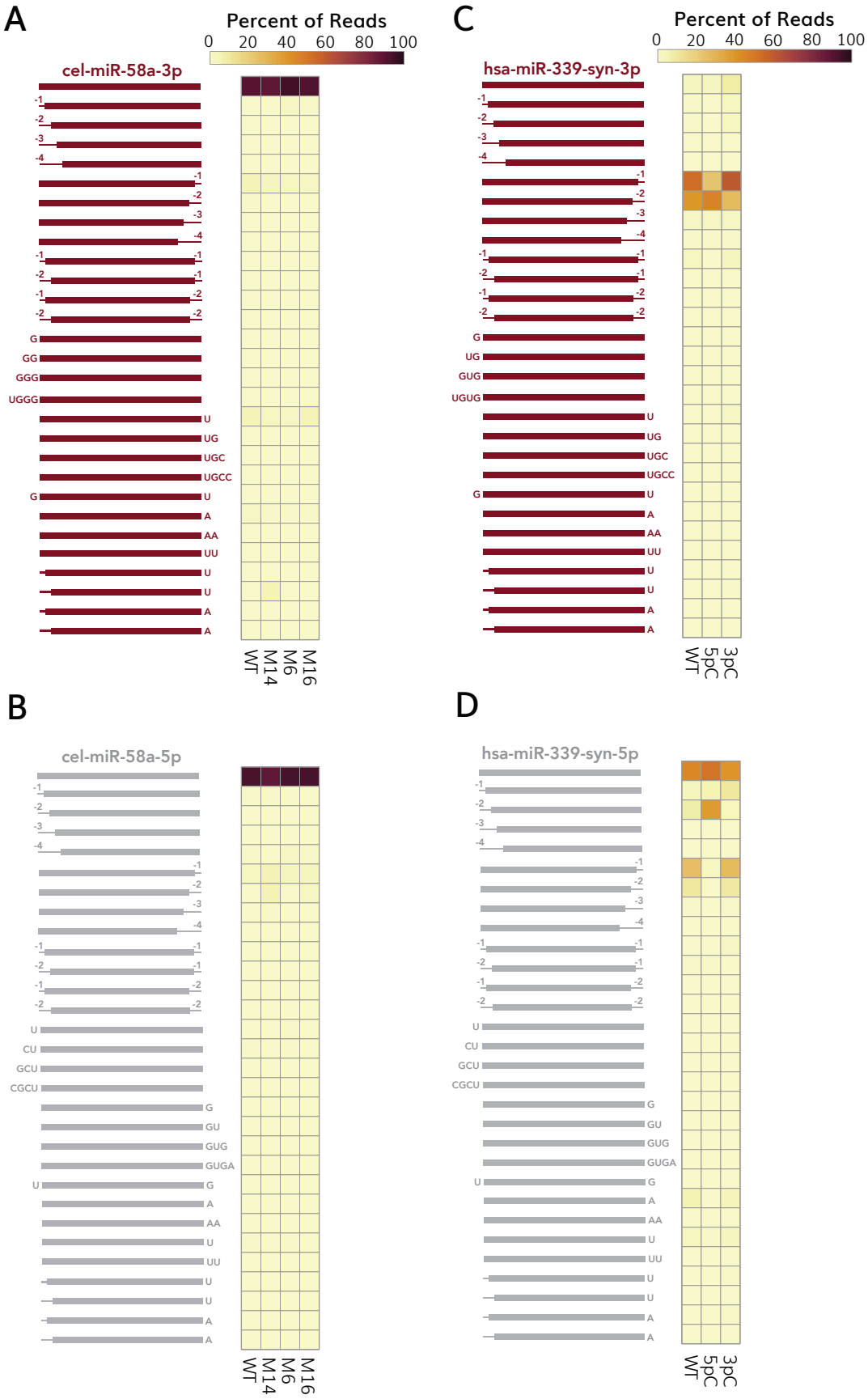

Extended Data Figure 10

A

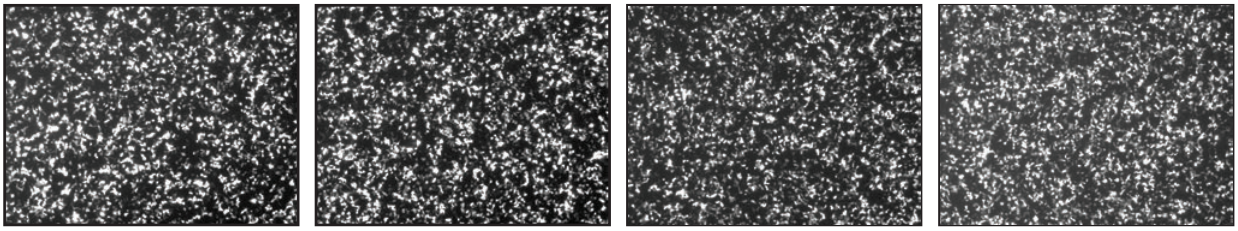

GFP siRNA control | hsa-miR-339-syn (pJM1) | cel-miR-58a-M6 (pJM2) | cel-miR-58a-M16 (pJM3)

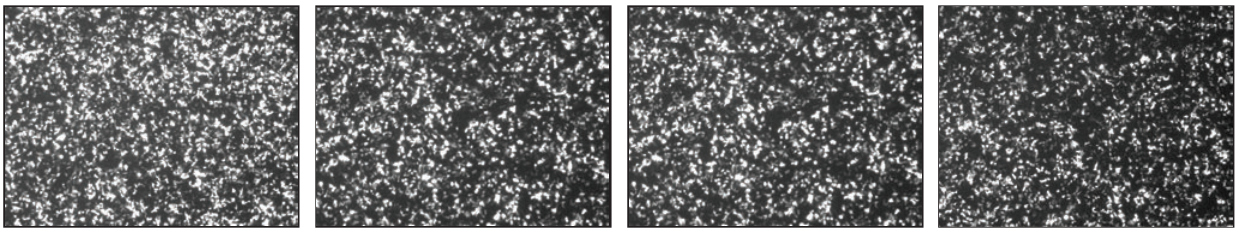

hsa-miR-339-syn-5pC (pJM4) | hsa-miR-339-syn-3pC (pJM5) | cel-miR-58a (pJM6) | cel-miR-58a-M14 (pJM7)

B

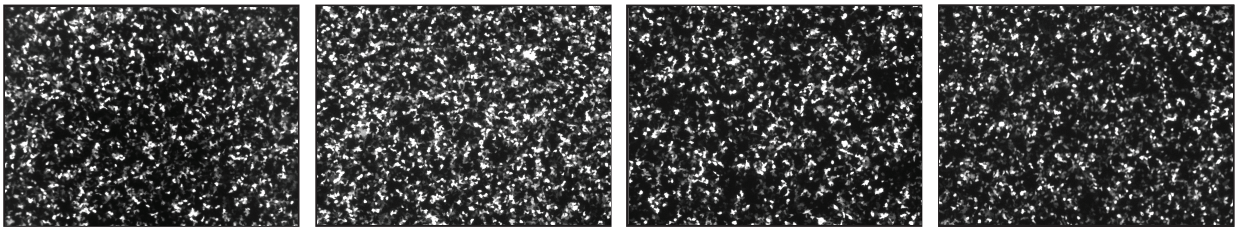

miR-58-M6_5pC-3pU (pJM2) | miR-58-M6_5pU-3pC (pJM3) | miR-58-M6_5pA-3pU (pJM10) | miR-58-M6_5pU-3pU (pJM11)

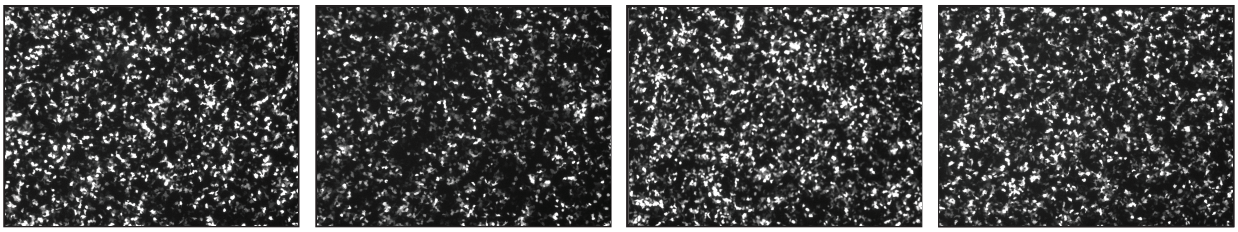

miR-58-M6_5pG-3pU (pJM12) | miR-58-M6_5pC-3pA (pJM13) | miR-58-M6_5pA-3pA (pJM14) | miR-58-M6_5pU-3pA (pJM15)

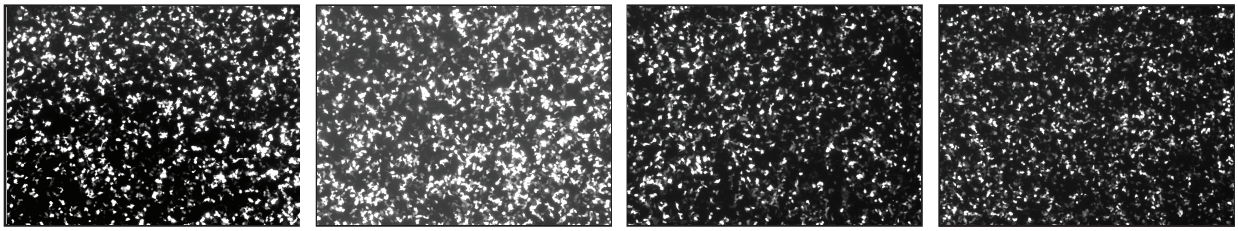

miR-58-M6_5pG-3pA (pJM16) | miR-58-M6_5pG-3pU (pJM17) | miR-58-M6_5pA-3pG (pJM18) | miR-58-M6_5pU-3pG (pJM19)

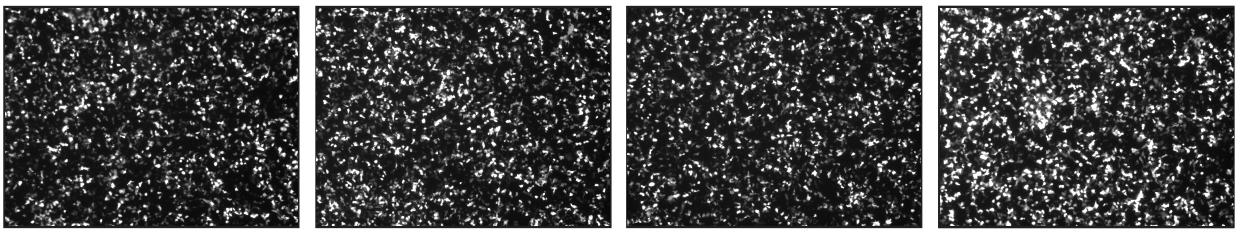

miR-58-M6_5pG-3pG (pJM20) | miR-58-M6_5pA-3pC (pJM21) | miR-58-M6_5pC-3pC (pJM22) | miR-58-M6_5pG-3pC (pJM23)

Supplementary Figure 1